Extensional flow of a free film of nematic liquid crystal with moderate elasticity ⊘

M. J. Taranchuk (ID) ; L. J. Cummings (ID) ; T. A. Driscoll (ID) ; R. J. Braun ✉ (ID)

Check for updates

View Online   Export Citation   CrossMark

Articles You May Be Interested In

From improving eyesight to disease theranostics: The impact of ocular fluid mechanics research

Physics of Fluids (August 2023)

Heat transfer and tear film dynamics over multiple blink cycles

Physics of Fluids (July 2014)

Features and examples of clustering in the system GeoBazaDannych

AIP Conference Proceedings (May 2023)

Physics of Fluids

AIP Publishing

Extensional flow of a free film of nematic liquid crystal with moderate elasticity

View Online　　Export Citation　　CrossMark

M. J. Taranchuk,[1] (iD) L. J. Cummings,[2] (iD) T. A. Driscoll,[1] (iD) and R. J. Braun[1,a)] (iD)

AFFILIATIONS

[1]Department of Mathematical Sciences, University of Delaware, Newark, Delaware 19716, USA
[2]Department of Mathematical Sciences, New Jersey Institute of Technology, Newark, New Jersey 07102, USA

Note: This paper is part of the special topic, Flow and the Eye.
[a)]Author to whom correspondence should be addressed: rjbraun@udel.edu

ABSTRACT

The human tear film is a multilayer structure in which the dynamics are often strongly affected by a floating lipid layer. That layer has liquid crystalline characteristics and plays important roles in the health of the tear film. Previous models have treated the lipid layer as a Newtonian fluid in extensional flow. Motivated to develop a more realistic treatment, we present a model for the extensional flow of thin sheets of nematic liquid crystal. The rod-like molecules of these substances impart an elastic contribution to the rheology. We rescale a weakly elastic model due to Cummings *et al.* ["Extensional flow of nematic liquid crystal with an applied electric field," Eur. J. Appl. Math. **25**, 397–423 (2014).] to describe a lipid layer of moderate elasticity. The resulting system of two nonlinear partial differential equations for sheet thickness and axial velocity is fourth order in space, but still represents a significant reduction of the full system. We analyze solutions arising from several different boundary conditions, motivated by the underlying application, with particular focus on dynamics and underlying mechanisms under stretching. We solve the system numerically, via collocation with either finite difference or Chebyshev spectral discretization in space, together with implicit time stepping. At early times, depending on the initial film shape, pressure either aids or opposes extensional flow, which changes the free surface dynamics of the sheet and can lead to patterns reminiscent of those observed in tear films. We contrast this finding with the cases of weak elasticity and Newtonian flow, where the sheet retains the same qualitative shape throughout time.

Published under an exclusive license by AIP Publishing. https://doi.org/10.1063/5.0151809

I. INTRODUCTION

The tear film of the eye is a thin multi-layer protective liquid film lying over the cornea. It is painted onto the ocular surface during the upstroke of the blink, and is re-formed rapidly after each blink.[1] Proper function of the tear film is essential for eye health and clear vision.[2] The most abundant component of the tear film is the aqueous layer, sandwiched between a mucin layer called the glycocalyx, that is bound to the ocular surface, and a thin lipid layer that floats on it. A sketch of a cross-section of a small part of the tear film is shown in Fig. 1. Proceeding toward the eye from the surrounding air, the first layer encountered is the lipid layer, which averages on the order of tens of nanometers thick.[3] Next comes the aqueous layer, which is typically a few micrometers thick,[4] and which contains large molecules such as soluble mucins and proteins.[5] The glycocalyx is a forest of membrane-bound mucins and associated molecules that form a protective barrier for the ocular surface.[6–9] Finally, the outer surface of the corneal epithelium is the beginning of the ocular surface itself.[10]

The normal tear film structure can fail to form initially, or sometime after a blink develop tear breakup, where the tear film fails to coat the ocular surface.[11,12] Tear breakup and associated hyperosmolarity (excessive saltiness of the local tears) is thought to play an important role in the development of dry eye disease, which affects millions of people.[13–15] The tear film lipid layer is of interest because it plays an important role in preventing tear breakup. Simultaneous imaging of the lipid layer and the aqueous layer[16] shows a strong correlation between lipid layer dynamics and tear breakup. The lipid layer is typically thought to be a barrier to evaporation, thus providing an important function to preserve the tear film between blinks.[17,18] However, the lipid layer composition[19] and structure[20–22] are complex and not yet fully understood. Meibum, an oily secretion from meibomian glands in the eyelids,[23] is the primary component of the lipid layer; it is not uncommonly used as a model for the lipid layer. X-ray scattering methods applied to *in vitro* meibum films have suggested that there are ordered particles in the meibum films with layered structures;[22] these particles may have liquid crystal structure. Hot-stage imaging of meibum droplets have shown birefringence,[19] another sign of order within the meibum. In the meibomian glands[23] in the human eyelid, freeze fracture with electron microscopy shows a layered structure of
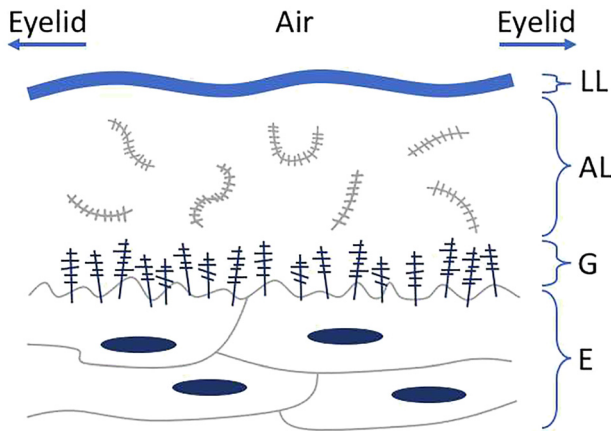
FIG. 1. A sketch of the tear film on the ocular surface. Here LL denotes the lipid layer, AL the aqueous layer, G the glycocalyx, and E is the outermost part of the corneal epithelium. The objects in the interior of the aqueous layer represent large mucin and protein molecules.

the lipids inside the cells that are the source of the meibum.[24] We interpret this evidence to suggest that the tear film lipid layer could be an extended liquid crystalline layer (possibly with defects).[25] It is not known whether the entire lipid layer has these qualities, or whether isolated chunks of structured particles float in the layer; however, there is general agreement that the lipid layer has non-Newtonian properties.[19,21,22,26,27] These areas of structure in the lipid layer are thought to provide the barrier against evaporation of the aqueous layer.[19,22] In addition, cooling of liquid crystals facilitates orientation of the molecules in the same direction.[28] The ocular surface cools about 1–$2\,^{\circ}\mathrm{C}$ during the interblink period when the eye is open,[29–31] and is heated during the blink; thus there is thermal cycling of the ocular surface as well as the mechanical cycling from blinks.[32,33] The cooling of the lipid layer may encourage the formation of liquid crystal structure *in vivo*.[20]

As the eye reopens during a blink, the lipid layer undergoes extensional flow as the tear film is painted across the surface of the eye.[1] Rather than spreading smoothly and uniformly over the eye, imaging of the tear film sometimes reveals stripes or ripples in the lipid layer (see Fig. 2).[1] The goal of this paper is to propose a minimal model for the lipid layer of the tear film (during the opening part of the blink cycle) as a thin sheet of liquid crystal in extensional flow. We will study both weak and moderate elasticity limits, and thereby lay

the foundation enabling us to explore whether such a model can replicate the type of rippling seen in the tear film.

Theoretical modeling of extensional flow was developed quite extensively in the twentieth century[34] and continues to be an active area of study, in part because of industrial applications such as optical fiber drawing[35] and the use of polymers for a wide range of industrial purposes. Thus, much work has been done on extensional flow of both Newtonian and non-Newtonian fluids, especially thin sheets or fibers. We do not attempt a comprehensive review here, but simply highlight a few studies of relevance to our problem. Evolution of Newtonian fibers under extensional flow has been studied extensively, from axisymmetric viscous fibers with one-dimensional flow by Schultz and Davis,[36] to more complicated three-dimensional models for non-axisymmetric fibers by Dewynne et al.[37,38] Wylie et al.[39] discuss the role of inertia and surface tension in the extensional flow of viscous fibers and study in particular, situations in which the effects of surface tension appear at higher order and can be neglected, but where inertia plays an important role in the evolution. Howell[35] presented several exact solutions for the extensional flow of both sheets and fibers of primarily Newtonian fluid (and also provides an excellent overview of earlier extensional flow modeling). Such flows are relevant for glass manufacturing, printing, and other applications; see also Dewynne et al.[38] for further discussion and references. Non-Newtonian fluids have also received attention; for example, the development of beads on a string has been described by Clasen et al.[40] for polymer fluids in a jet or liquid bridge and by Sostarecz and Belmonte[41] for micellar fluid under stretching, while Smolka et al.[42] presented an exact solution for the extensional flow of a thread of fluid under both weakly and strongly viscoelastic limits. Most relevant to our application, however, Cummings et al.[43] studied extensional flow of sheets of nematic liquid crystals, and this is the scenario on which we now focus, as we hope it can shed light on the dynamics of the tear film of the eye during the blink cycle.

As a starting point, we use the model of Cummings et al.,[43] which uses the Ericksen–Leslie equations to describe extensional flow of a thin sheet of nematic liquid crystal. The main focus of that paper is the response of the liquid crystal film to an applied electric field (relevant to many technological applications, such as electronic displays). In a biological setting such as the human eye, however, no electric field is present, thus, we neglect this aspect of the modeling but follow the same asymptotic approach. We rescale the governing equations and consider a new limit for the case of moderate elastic effects. The scaling is based on those developed for nematic thin films on a substrate studied by Lin et al.[44] and Lam et al.[45] The application to the extensional
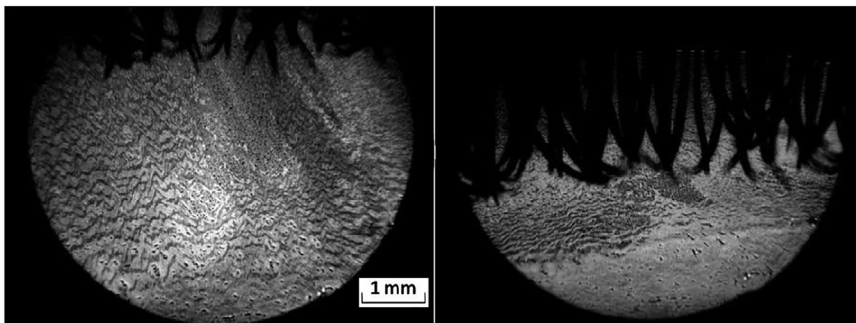

FIG. 2. Ripples in the lipid layer of the tear film before a blink (left), and after a blink (right). The ripples become compressed during a blink, and may not extend to cover the cornea once the eye is open.[1] A version of this figure was published in Ref. 1. Reproduced with permission from Braun et al., Prog. Retinal Eye Res. **45**, 132–164 (2015). Copyright 2015 Elsevier.
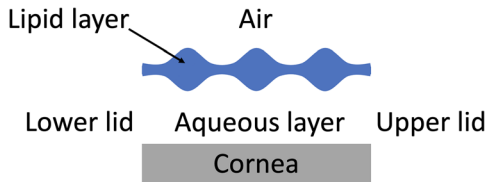
FIG. 3. Simplified sketch of a cross section of the tear film.

case is new, to our knowledge. We analyze a range of different boundary conditions imposed at the sheet's ends, which are found to strongly affect the shape of the evolving sheet under stretching. We then investigate rippling dynamics in the sheet by varying the number of waves in the initial condition.

The paper is organized as follows. In Sec. II we describe the problem formulation, and present the mathematical models for both weak and moderate elasticity. Section III provides details of the numerical methods used to solve the models. In Sec. IV we present our results. These include profiles of the sheet thickness, fluid velocity, and film pressure that result from the different boundary conditions. We compare and contrast the solutions obtained under weak and moderate elasticity, when either the surface tension or speed of the moving end is varied. Then we present results when multiple waves are added to the initial condition, and the mechanisms for the observed dynamics. Finally, in Sec. V we discuss the results and outline our conclusions.

II. MODELS

To reduce the complexity of the lipid layer geometry seen in Fig. 1, we simplify the cross section of the tear film (the sagittal plane) to the geometry shown in Fig. 3, where the ripples in the lipid layer of the tear film appear in a 2D configuration of waves with varying thickness. This geometry is suggested by the variations in layer thickness seen *in vivo* from imaging experiments[1] like those of Fig. 2. In this work, we neglect the aqueous layer, and consider the lipid layer alone, in two dimensions. Thus, as a first step, we consider it to be a thin free film in a sheet configuration, with multiple waves on the fluid/air interfaces in the initial condition.

The sheet of fluid is assumed fixed at the left end, while the right end moves with a prescribed constant speed v_0, providing a simple model of the opening eyelid following a blink. A sketch is shown in Fig. 4. As a further simplification, the lipid sheet is assumed symmetric about its midline, which is assumed to be straight. We denote the thickness of the sheet by $h(x, t)$, the axial fluid velocity by $u(x, t)$, and the transverse velocity by $w(x, t)$. The liquid crystal molecules in the lipid sheet are assumed to have a preferred angle of θ_B relative to $\hat{n}$,
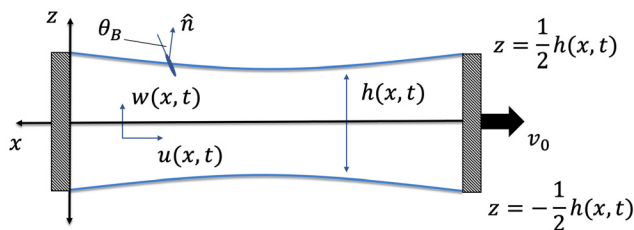
the outward-facing unit vector normal to the sheet surface. The angle of the molecules within the sheet is described by the director field $\mathbf{n} = (\sin\theta, \cos\theta)$; discussed further in the Appendices.

A. Weak elasticity

Our approach follows that of Cummings et al.,[43] who used multiple scale perturbation methods to simplify the Ericksen–Leslie equations[46] governing nematic liquid crystal dynamics. The Ericksen-Leslie equations [see Eqs. (A1)–(A4) of Appendix A] are nondimensionalized using the scalings given below, where primes denotes dimensional quantities. The coordinates (x', z') and velocity components (u', w') correspond to the axial and transverse directions respectively, h' represents the sheet thickness, t' is time, and p' is pressure:

$$x' = Lx, \quad z' = \delta Lz, \quad u' = \hat{U}u, \quad w' = \delta\hat{U}w, \quad (1)$$

$$h' = \hat{h}\delta Lh, \quad t' = \frac{L}{\hat{U}}t, \quad p' = \frac{\mu\hat{U}}{L}p. \quad (2)$$

As a result of these scalings, we define the non-dimensional (weak elasticity) surface tension number as

$$S_w = \frac{\delta}{\mu\hat{U}}\gamma', \quad (3)$$

where γ' is the surface tension at the film/air interface. This definition of S_w applies for all results in the weak elasticity limit.

The dimensional parameters used in the model are defined in Table I, along with the non-dimensional parameters that result from the chosen scalings. Asymptotic expansion of the dependent variables in the small parameter $\delta = \hat{h}/L$ (see Subsection 3 of Appendix A), yields a closed system of equations for the (leading order) sheet thickness h and axial velocity u

$$h_t + (hu)_x = 0, \quad (4)$$

$$\frac{F(\theta_B)}{G(\theta_B)}(hu_x)_x + \frac{S_w}{2}hh_{xxx} = 0. \quad (5)$$

TABLE I. Parameters used in the model scalings for weak elasticity. Different scales for S_w and $\hat{N}_w$ are used in the moderate elasticity model; see Eq. (11). Note that $\hat{N}_w$, δ, and S_w are dimensionless.

Parameter	Value (units)	Description
μ	0.037 (N s m^{-2})	Dynamic viscosity[47]
$\hat{U}$	0.01 (m s^{-1})	Typical axial velocity[48]
L	0.001 (m)	Typical sheet length[48]
$\hat{h}$	2.5×10^{-7} (m)	Typical initial sheet thickness[1]
γ'	0.031 (N m^{-1})	Surface tension of air/sheet interface[49]
K	6×10^{-12} (N)	Elastic constant of the liquid crystal[47]
$\delta = \dfrac{\hat{h}}{L} \ll 1$	2.5×10^{-4}	Aspect ratio
$S_w = \dfrac{\delta}{\mu\hat{U}}\gamma'$	0.02	Surface tension/viscosity comparison
$\hat{N}_w = \dfrac{K}{\mu\hat{U}\delta L}$	0.065	Inverse Ericksen number

FIG. 4. Schematic of a sheet of nematic liquid crystal stretched between two plates (further details in the text).

Equation (4) represents conservation of mass, and Eq. (5) is the axial force balance. The first term in Eq. (5) represents internal, viscous forces due to extension; these balance with the capillary forces represented by the second term. The coefficient of the first term is formed from functions $F(\theta_B)$ and $G(\theta_B)$, which depend in general on material properties of the fluid as well as the leading order solution for the director angle, θ_0 [see Eqs. (A22) and (A23) in Appendix A]. However, in the situation considered here, $\theta_0 = \theta_B$ is a fixed angle, and F and G are themselves also constant. If the properties of a Newtonian fluid are used, then $F/G = 4$, and Eq. (5) simplifies to

$$4(hu_x)_x + \frac{S_w}{2}hh_{xxx} = 0. \qquad (6)$$

For the remainder of this paper, we use this coefficient value of 4 when presenting weak elasticity solutions. We note that for the weak elasticity scalings chosen here, the pressure is defined as[43]

$$p = -2u_x - \frac{S_w}{2}h_{xx}. \qquad (7)$$

Whenever the pressure is shown for solutions to the weak elasticity model, we make use of Eq. (7). The Newtonian limit, with zero surface tension $S_w = 0$, becomes the Trouton model,[50] considered extensively within a Newtonian framework by Howell[35] (see also references therein).

The tension $T(t)$ in the sheet is found by taking the first integral of the axial force balance in Eq. (6), which gives

$$T(t) = 4hu_x + \frac{S_w}{2}\left(hh_{xx} - \frac{1}{2}h_x^2\right). \qquad (8)$$

In the absence of axial inertia, the tension is spatially uniform throughout the sheet (independent of x).[35]

Since we specify the speed of the moving end, we impose the following boundary conditions (BCs), where $s(t) = 1 + v_0 t$ denotes the location of the moving end,

$$u(0, t) = 0, \quad u(s(t), t) = v_0, \qquad (9)$$

$$h_x(0, t) = 0, \quad h_x(s(t), t) = 0. \qquad (10)$$

Typically, we take $v_0 = 1$ (consistent with our chosen scalings), with the exception of Sec. IV E, where we explore varying the speed of the moving end. Neumann BCs on h specify the contact angle of the film with the end plates; the plates are assumed to have no effect on the director field.

For the weak elasticity case, we solve the system of partial differential equations (PDEs) found in Eqs. (4) and (6), subject to the BCs in Eqs. (9) and (10), as well as given initial conditions (ICs) for $h(x, 0)$ and $u(x, 0)$ discussed below.

B. Moderate elasticity

To consider the case of moderate elasticity, we rescale the pressure to be one order larger while keeping the scalings for the other variables the same. As a result, the inverse Ericksen number, and the surface tension number S are also redefined as follows:

$$p' = \frac{\mu U}{\delta L}p, \quad \hat{N} = \frac{K}{\mu \hat{U}L}, \quad S = \frac{\delta^2}{\mu \hat{U}}\gamma'. \qquad (11)$$

Here primes denote dimensional quantities. Following the derivation outlined in Subsection 3 of Appendix A, we find the leading order pressure

$$p = -\frac{S}{2}h_{xx}, \qquad (12)$$

and obtain the following system

$$h_t + (hu)_x = 0, \qquad (13)$$

$$(hu_x)_x + \tilde{S}(h^2 h_{xxx})_x = 0, \qquad (14)$$

where $\tilde{S} = C_2(\theta_B)/B_2(\theta_B)S$ is the scaled surface tension with the scale factors B_2 and C_2 given in Eqs. (A55) and (A56) of Appendix A. For simplicity, we take $\tilde{S} = S$ in our computational solutions. In this case of moderate elasticity, the tension in the sheet is now given by

$$T(t) = hu_x + Sh^2 h_{xxx}. \qquad (15)$$

Although the surface tension at the lipid layer/air interface of the tear film is unknown, we use a value based on surface tension measurements for the nematic liquid crystal 5CB at a range of temperatures surrounding $35°\,C$,[51] which is close to the temperature at the surface of the eye.[52] Unless otherwise noted, we take $S = 0.025$.

We note that Eq. (14) is higher order than the analogous equation for the weak elasticity or Newtonian cases;[35,43] this change will be consequential for the dynamics of the film. To determine the number of boundary conditions needed we use Eq. (15) to eliminate hu_x from Eq. (13), yielding

$$h_t + uh_x + T(t) - Sh^2 h_{xxx} = 0. \qquad (16)$$

The highest derivative in this equation is third order, implying that we need three boundary conditions on h to solve the system; thus, we will need an additional boundary condition apart from those given in Eqs. (9) and (10).

1. Reducing the order

To solve the model numerically, it is preferable to reduce the order of the system by adding a dependent variable. We can add the pressure, p, shown in Eq. (12) to our system of PDEs as an additional dependent variable, and substitute into the axial force balance Eq. (14) to reduce the order of the highest derivative appearing in the system. We obtain

$$h_t + (hu)_x = 0, \qquad (17)$$

$$(hu_x)_x - (h^2 p_x)_x = 0, \qquad (18)$$

$$p + \frac{S}{2}h_{xx} = 0. \qquad (19)$$

Using this substitution, we can write the equation for tension in the moderate elasticity case [see Eq. (15)] as

$$T(t) = hu_x - h^2 p_x. \qquad (20)$$

The space-dependent terms on the right hand side of this equation combine to be independent of x.

2. Boundary and initial conditions

The boundary conditions for the axial velocity u are as in Eq. (9) for the weak elasticity case: $u(0, t) = 0$ and $u(s(t), t) = v_0$. For the

sheet thickness h three boundary conditions are required in this moderate elasticity case: we consider five such sets of boundary conditions, summarized in Table II. In all cases, the third (additional) boundary condition on h is enforced by setting $p_x(0, t) = 0$ on the fixed end, as discussed below.

Turning to Table II, cases I and II specify Neumann conditions (homogeneous and non-homogenous) on h. Cases III and IV specify a Robin condition on the right (moving) or left (fixed) end respectively. Case V specifies Robin conditions on both ends of the domain. The parameter ν may vary between 0 and 1; a smaller value for ν results in a boundary condition that is close to a pure Dirichlet condition at that end. In the physical sense, the Robin boundary conditions model capillarity on one end of the sheet. A Dirichlet condition would represent fluid pinned to the plate, with the slope free to vary. The Neumann conditions specify the contact angle formed by the liquid crystal fluid and the plate, but the thickness of the film is free to vary. Homogeneous Neumann conditions represent a contact angle of $\pi/2$.

Our final choice of boundary condition in this moderate elasticity case is motivated by the tension equation Eq. (20). To do this, we take an initial condition, compute all the terms in the tension, then examine the value of each term at the boundary. As an example, for the initial condition $h(x, 0) = 0.9 + 0.1 \cos(2\pi x)$, we first find $u(x, 0)$ by solving Eq. (14) subject to $u(0, 0) = 0$ and $u(1, 0) = v_0$ with $S = 0.025$ and $v_0 = 1$. To find the initial pressure $p(x, 0)$, the definition in Eq. (19) is used. We then plot the individual terms from Eq. (20) [or equivalently, Eq. (15)]. These curves result from compatible boundary and initial conditions for which we present solutions below. We see that one component of the tension, $h^2 p_x$, is zero at the left end, which implies that $p_x(0, 0) = 0$. We have generalized this observation to impose $p_x(0, t) = 0$ as a third boundary condition in all of our computations. Attempts to instead impose the third boundary condition at the right end of the domain cause instability in our simulations, which suggests that the PDE has a right-going characteristic, although we have not proven this. Taking this empirical evidence together, we choose to enforce $p_x(0, t) = 0$ as the additional boundary condition at $x = 0$ for the moderate elasticity model. In physical terms, Fig. 5 shows that, at $x = 0$, all of the tension is in the extensional term while none is in the pressure term.

The initial condition for h is chosen as

$$h(x, 0) = a + b \cos(2\pi k_0 x) + c\, x(x - 1). \qquad (21)$$

TABLE II. Summary of boundary conditions on a moving domain with an initial condition $h(x, 0) = a + b \cos(2\pi k_0 x) + c\, x(x - 1)$, and $0 < \nu < 1$. The quadratic term in the initial condition is only used in case II.

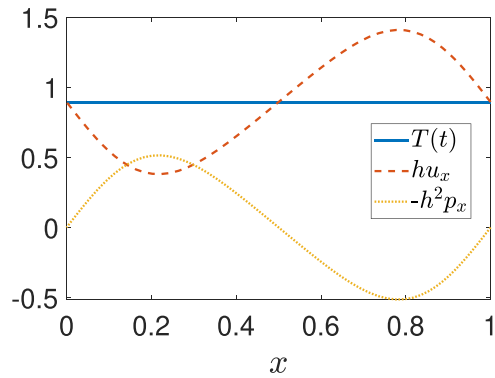| Case	Fixed end, $x = 0$	Moving end, $x = 1 + v_0 t$	a	b	c
I	$h_x = 0, \quad p_x = 0$	$h_x = 0$	0.9	0.1	0
II	$h_x = -c, \; p_x = 0$	$h_x = c$	0.9	0.1	0.1
III	$h_x = 0, \quad p_x = 0$	$(1 - \nu)(h - 1)$ $+ \nu h_x = 0$	0.9	0.1	0
IV	$(1 - \nu)(h - 1) - \nu h_x = 0,$ $p_x = 0$	$h_x = 0$	0.9	0.1	0
V	$(1 - \nu)(h - 1) - \nu h_x = 0,$ $p_x = 0$	$(1 - \nu)(h - 1)$ $+ \nu h_x = 0$	0.9	0.1	0

FIG. 5. The tension $T(t)$ and its component terms from Eq. (20) are plotted at $t = 0$ for $h(x, 0) = 0.9 + 0.1 \cos(2\pi x)$. See text for further discussion.

The wavenumber k_0 will typically be $k_0 = 1$ but will be systematically varied in later sections. The quadratic term ($c \neq 0$) is used only in BC case II, where we allow a nonzero slope at the ends. The initial condition for p is calculated exactly via Eq. (18). We also solve for $u(x, 0)$ in order to have a consistent initial condition for the numerical solvers that we use. We return to this point in Sec. III below.

We note that the tear film volume (area) remains constant for all choices of our BCs to within the tolerances specified for the numerical methods. Analytically, this must be true due to the boundary conditions on u; at the ends, the fluid must travel with the same speed which does not allow fluid to cross the boundaries.

III. NUMERICAL SOLUTION

To solve the models numerically, we first map from a moving domain $0 < x < s(t)$ with $s(t) = 1 + v_0 t$, to a fixed domain $0 < \xi < 1$ using $\xi = x/s(t)$. On the fixed domain, the unknowns become $H(\xi, t) = h(x, t)$ and $U(\xi, t) = u(x, t)$. We apply this mapping to both the weak and moderate elasticity models.

A. Weak elasticity

After mapping Eqs. (4), (5), (9), (10), and (21) to the fixed domain, one obtains

$$H_t - v_0 \frac{\xi}{s} H_\xi + \frac{1}{s}(UH)_\xi = 0, \qquad (22)$$

$$4(U_\xi H)_\xi + \frac{S}{2s} HH_{\xi\xi\xi} = 0, \qquad (23)$$

$$H_\xi(0, t) = 0, \quad H_\xi(1, t) = 0, \qquad (24)$$

$$U(0, t) = 0, \quad U(1, t) = v_0, \qquad (25)$$

$$H(\xi, 0) = a + b \cos(2\pi k_0 \xi) + c\xi(\xi - 1). \qquad (26)$$

Note that for this model there are only two BCs for h and two BCs for u;[43] we do not impose the BC on p.

B. Moderate elasticity

For the moderate elasticity case, the problem defined in Eqs. (17), (18), (19), and (21), along with the boundary conditions for BC case III, becomes

$$H_t - v_0 \frac{\xi}{s} H_\xi + \frac{1}{s}(UH)_\xi = 0, \tag{27}$$

$$(U_\xi H)_\xi - (H^2 P_\xi)_\xi = 0, \tag{28}$$

$$P + \frac{S}{2s^2} H_{\xi\xi} = 0, \tag{29}$$

$$H_\xi(0,t) = 0, \; P_\xi(0,t) = 0, \; (1-\nu)sH(1,t) + \nu H_\xi(1,t) = 0, \tag{30}$$

$$U(0,t) = 0, \quad U(1,t) = v_0, \tag{31}$$

$$H(\xi,0) = a + b\cos(2\pi k_0 \xi) + c\xi(\xi - 1). \tag{32}$$

Boundary condition case I is recovered by setting $\nu = 1$ in case III here, while cases II, IV, and V are transformed similarly.

C. Numerical methods

We describe the implementation for the moderate elasticity case here in detail; the weak elasticity case is treated similarly. After mapping to a fixed domain, we apply a version of the method of lines; we implement two approaches to validate our results. The spatial derivatives are approximated via collocation with either finite difference or Chebyshev spectral discretization. When utilizing finite difference methods, we use a uniform grid. Second-order centered formulas are used inside the domain, and the appropriate second-order non-centered formulas are used to approximate the derivatives at the left and right ends of the sheet. The result is a system of differential algebraic equations (DAEs) at the grid points that we solve forward in time in MATLAB (MathWorks, Natick, MA, USA) using `ode15s`. In general, the number of grid points is $N = 512$. As a check, we use the trapezoidal method to calculate the fluid volume, and observe that it is conserved to the order of our imposed tolerances of 10^{-4}.

Alternatively, we use Chebyshev spectral discretization in space, which also results in a DAE system solved in the same way.[53] Typically, the number of grid points we used was $N = 128$ for this method.

For either approach, the initial sheet thickness $h(x, 0)$ was first specified, then $p(x, 0)$ computed from its definition in Eq. (19). Finally, the discrete version of the axial force balance Eq. (18) was solved for u on the grid points using the backslash.

The results using both methods agree, until the final times when error accumulates at the ends of the domain with the finite difference method. However, the spectral method could not complete computations over as wide a range of parameter values (for example, for surface tension) as could the finite difference method. Validation data are given in Appendix B.

IV. RESULTS

We begin by showing solutions for thickness and velocity for the simple case of an initially flat sheet. We then present solutions for thickness, velocity, and pressure obtained for the various boundary conditions outlined in Table II in the case of moderate elasticity, and we compare them with the corresponding results in the case of weak elasticity (where the condition $p_x(0, t) = 0$ is not used). We note how the location of the sheet's minimum thickness changes depending on the boundary conditions imposed. Next, we vary both the surface tension and speed of the moving end, and demonstrate the effect for both moderate and weak elasticity. We investigate dynamics resulting from increasing the number of sinusoidal waves in the initial condition, and

show examples of how the wave profile changes through time depending on the surface tension value, and the amplitude and period of the imposed initial waves. Finally, we discuss possible mechanisms responsible for those dynamics.

A. Neumann conditions on h

We begin by showing solutions for an initially flat sheet. We take $h(x, 0) = 1$, with BC case I given by $h_x(0, t) = h_x(1, t) = 0$, $u(x, 0) = v_0 x$, $u(0, t) = 0$, and $u(1, t) = v_0 = 1$. In this scenario, the sheet remains spatially uniform for all time, and the PDEs governing h and u for both weak and moderate elasticity are the same, as the terms containing surface tension are lost. Solutions for h and u are shown in Fig. 6 on the moving domain. The thickness decreases uniformly, and the velocity increases linearly across the sheet. Note that $p_x = 0$ trivially for all x and t for both moderate and weak elasticity models. In the case of moderate elasticity, the pressure is zero at each time level. In the case of weak elasticity, from Eq. (7), $p = -2u_x$ and so p is constant in x but decreasing in time.

Next, we consider the moderate elasticity solutions for the sheet thickness, axial velocity, and pressure when $S = 0.1$ for a sinusoidal IC with $a = 0.9$, $b = 0.1$, and $c = 0$. Results are shown in Fig. 7. Initially, the axial velocity is negative for much of the sheet, meaning that the fluid in these areas is moving to the left. This changes the profile of the sheet thickness very quickly, and extensional flow leads to thinning of the sheet at the right end. The fluid away from the right end is left behind, and by $t = 0.25$, there is no longer a local maximum in the thickness at the right end. From that time until $t = 3$, the sheet thickness has lost approximately half a wave from the initial one full period.

The tendency of fluid to gather at the left end while the right end becomes thinner is a characteristic of moderate elasticity that is not seen in the case of weak elasticity. Figure 8 shows the analogous solutions for h, u and p of a sheet of fluid with weak elasticity. The sheet remains symmetric about its midpoint throughout the computation, and $h_{\min}$ occurs in the middle of the sheet. The middle plot of Fig. 8 shows that as time progresses, the strain rate u_x is largest in the middle of the sheet, and the sheet thins fastest there. The pressure remains negative throughout the sheet, but the absolute values of the pressure and their gradients decrease as time increases.

B. Robin boundary conditions (moderate elasticity)

Imposing a Robin boundary condition at the moving end (BC case III) of a sheet with moderate elasticity leads to the formation of a
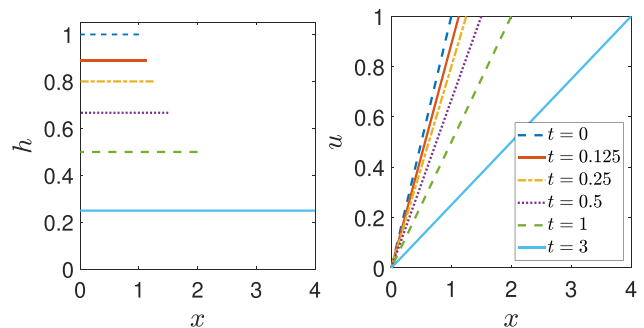

FIG. 6. Profiles of sheet thickness, h, and fluid velocity, u, for an initially flat sheet with homogeneous Neumann boundary conditions and $v_0 = 1$.
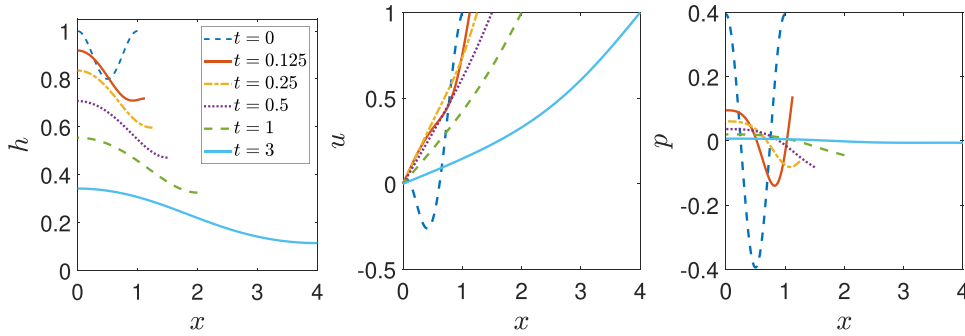
FIG. 7. Profiles of sheet thickness, h, fluid velocity, u, and pressure, p, for moderate elasticity with a sinusoidal IC and BC case I when $S = 0.1$ and $v_0 = 1$.
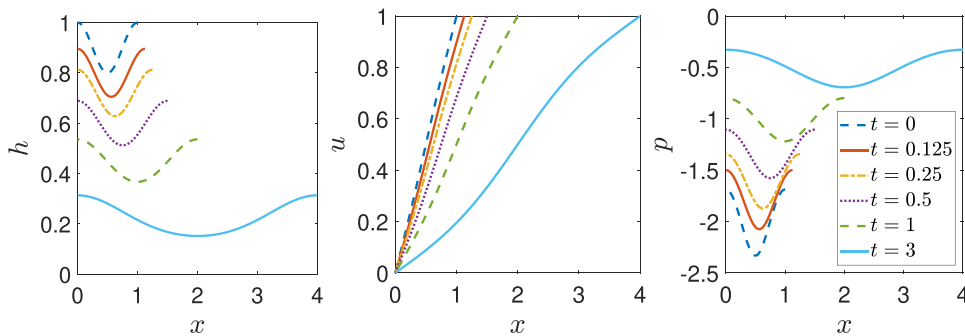

FIG. 8. Profiles of sheet thickness, h, fluid velocity, u, and pressure, p, for weak elasticity with a sinusoidal IC and BC case I when $S = 0.1$ and $v_0 = 1$.
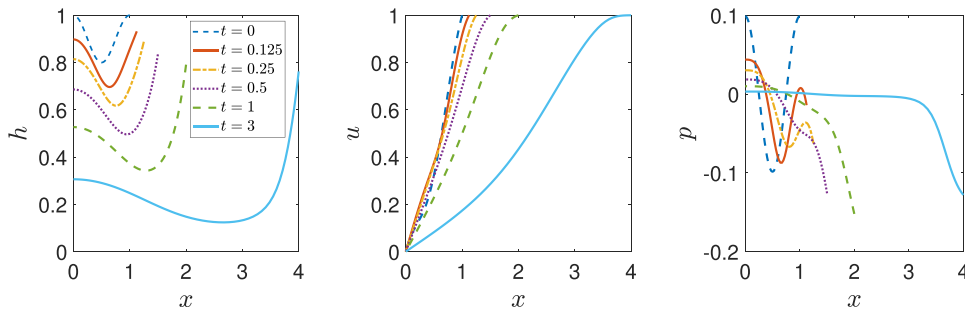

FIG. 9. Profiles of sheet thickness, h, fluid velocity, u, and pressure, p, for moderate elasticity with BC case III, a Robin boundary condition at the right end; $\nu = 0.1$, $S = 0.025$, and $v_0 = 1$.

meniscus there, as shown in Fig. 9. The sheet thins primarily in the middle and left (fixed) end of the sheet, with a narrow portion of the fluid at the right traveling at roughly the same speed as the right (moving) end. The pressure remains positive at the left end due to capillarity, but becomes negative throughout the part of the sheet that forms the meniscus.

Figure 10 shows the results of imposing a Robin condition at the fixed end on the left (BC case IV). This meniscus is smaller in both height and width than that of Fig. 9, where the Robin condition is imposed at the right. As observed in Fig. 9, thinning corresponds to increased strain rate u_x in the portion of the sheet where it occurs. As time increases the meniscus grows, and the pressure becomes
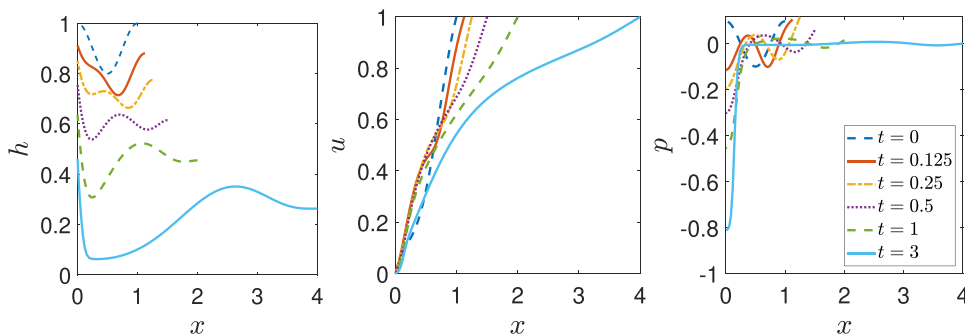

FIG. 10. Profiles of sheet thickness, h, fluid velocity, u, and pressure, p, for moderate elasticity with BC case IV, a Robin boundary condition at the left end; $\nu = 0.1$, $S = 0.025$, and $v_0 = 1$.

TABLE III. Comparison of imposing Robin boundary conditions at either and both ends of the sheet. Here h_{max} is the maximum sheet thickness, h_{min} is the minimum sheet thickness, and $\Delta h = h_{max} - h_{min}$.

Robin location	$t = 0.5$			$t = 4$		
	h_{max}	h_{min}	Δh	h_{max}	h_{min}	Δh
Right end (BC case III, Fig. 9)	0.835	0.497	0.338	0.763	0.086	0.676
Left end (BC case IV, Fig. 10)	0.758	0.538	0.220	0.431	0.037	0.394
Both ends (BC case V, Fig. 11)	0.835	0.502	0.333	0.811	0.027	0.785

large and negative at $x = 0$, while approaching zero in the rest of the film.

Table III summarizes the differences: in both cases, the maximum sheet thickness h_{max} occurs at the end where the Robin condition is enforced. When the condition is enforced at the left (BC case IV), both h_{max} and the range of observed sheet thicknesses ($\Delta h = h_{max} - h_{min}$) are smaller, and at the final time $t = 4$, h_{min} is less than half the corresponding value when the Robin condition is imposed at the right (BC case III).

Finally, imposing a Robin boundary condition on both ends (BC case V) of a sheet with moderate elasticity generates an additional wave which is slowly lost as the sheet stretches, as shown in Fig. 11. The sheet thins more at the left (fixed) end of the sheet, with fluid accumulating at the right (moving) end. The thin region near the fixed end extends for roughly a third of the length of the film at the final time.

C. Location of minimum thickness

As mentioned before, in the weak elasticity case, the evolution of the sheet is symmetric about the midpoint for the chosen boundary and initial conditions. The minimum sheet thickness h_{min} begins, and remains, at the midpoint throughout the evolution. For moderate elasticity, however, the situation is more complicated. Figure 12 summarizes a range of results for different BCs, with the initial condition $h(x, 0) = a + b\cos(2\pi x)$ with $a = 0.9$, $b = 0.1$ (as used in the results of Secs. IV A and IV B above), and $S = 0.025$ unless otherwise noted. Figure 12 demonstrates that, even with a simple initial film shape that is initially symmetric about the midpoint, the minimum thickness migrates from the midpoint, and can occur in a variety of locations on
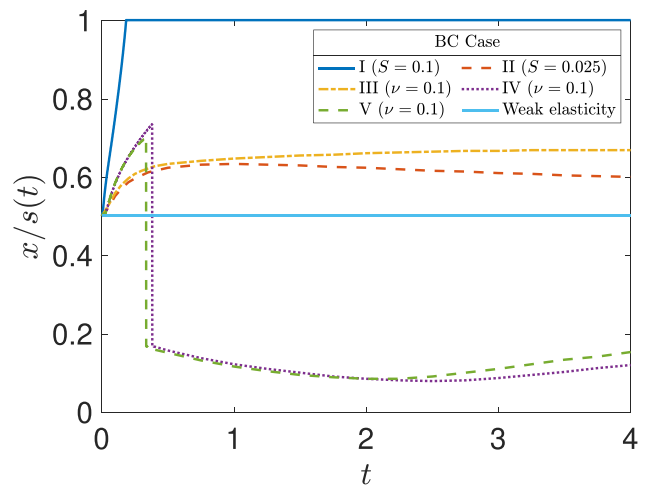

FIG. 12. Location of minimum sheet thickness shown on a fixed domain through time. In all cases, $h(x, 0) = 0.9 + 0.1\cos(2\pi x)$, and $S = 0.025$ except where otherwise stated. In BC case II, $c = 0.1$ (see Table II).

the sheet that depend on the boundary conditions imposed. If we consider BC case I (homogeneous Neumann conditions on h), with $S = 0.1$, then the minimum rapidly migrates to the right end of the domain, by about $t = 0.25$. For BC case I with $S = 0.025$ (not shown in Fig. 12), the minimum remains in the right half of the domain near $x = 0.5$. Allowing a slight slope on the end (BC case II, with $c = 0.1$) keeps the minimum slightly more centered than BC case I for the same S. With $S = 0.025$ and BC cases I and II, the minimum starts in the center of the sheet (as dictated by the initial condition), shifts to the right by $t = 0.15$ or so, and then slowly begins to approach the center of the sheet again. A Robin boundary condition on the right (BC case III) leads to a minimum location that begins similarly to BC case I: the minimum shifts to about $\xi = x/s(t) = 0.7$, but then stays there. A Robin boundary condition on the left (BC case IV) causes the location of the minimum to move around the most. Referring to Fig. 10, we see that for early times, the sheet has two local minima, with the global minimum closest to the moving end. As the sheet lengthens, that dip flattens, and the global minimum shifts to the bottom of the steep meniscus near the fixed end. For the remaining time, the minimum stays close to the left (fixed) end. This switch in the location of the global minimum is clearly seen in Fig. 12. Robin boundary conditions on both ends (BC case V) leads to a minimum location pattern that closely follows that of BC case IV.
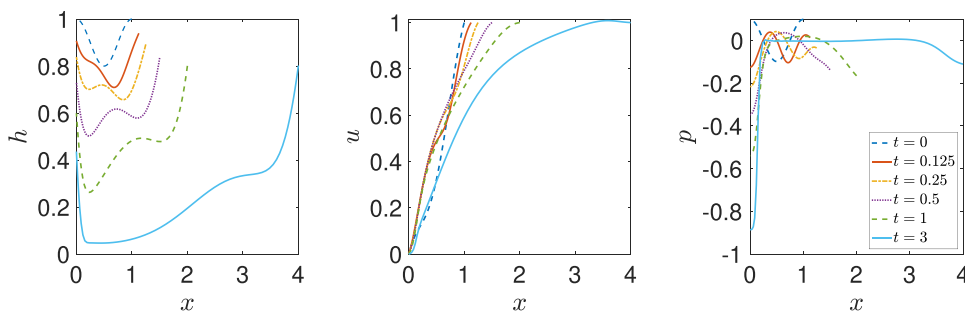

FIG. 11. Profiles of sheet thickness, h, fluid velocity, u, and pressure, p, for moderate elasticity with BC case V, Robin boundary conditions at both ends; $\nu = 0.1$, $S = 0.025$, and $v_0 = 1$.
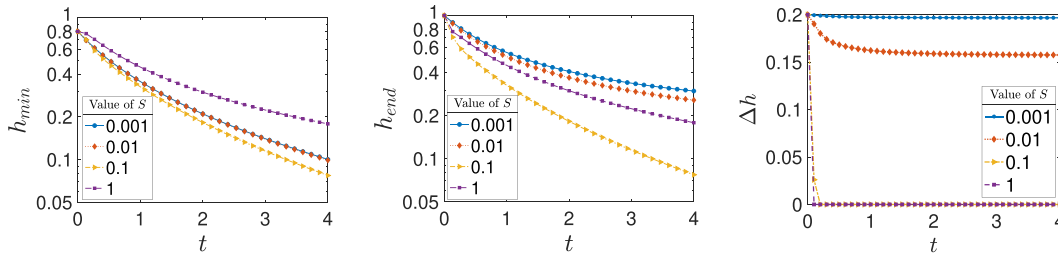
FIG. 13. Evolution of the minimum sheet thickness, h_{min}, thickness h_{end} at the right end of the sheet, and $\Delta h = h_{end} - h_{min}$, as the surface tension varies for moderate elasticity. Results are for BC case I with $v_0 = 1$. In the left plot, the curve for $S = 0.001$ (in blue) lies directly under that of $S = 0.01$ (in red).

D. Varying the surface tension (moderate elasticity)

We summarize the effect of the surface tension γ on the sheet thickness for the moderate elasticity model in Fig. 13, where we compare a range of S-values, spanning four orders of magnitude. The first plot of Fig. 13 shows the minimum sheet thickness h_{min} vs time t on a semilog scale. The relationship between h_{min} and S is not monotone; the largest values of h_{min} for all values of time occur when surface tension is largest ($S = 1$), while the smallest values occur at $S = 0.1$. Smaller values of S lead to intermediate minimum thickness values. The second plot of Fig. 13 shows the film thickness at the right end of the sheet, $h_{end} = h(s(t), t)$, vs t, on a semilog scale. The minimum thickness may occur at the right end (see Fig. 7).

E. Varying the speed of the moving end

In the previous results, we varied surface tension number S, while fixing the speed of the moving end at $v_0 = 1$. Now we vary the speed, for fixed surface tension number $S = 0.025$. Figures 14 and 15 show, for moderate and weak elasticity respectively, how the sheet thickness (as characterized by h_{min} and h_{end}) is affected when v_0 varies from 0.25 to 2.5. The plots show h_{min} and h_{end} vs time t, on a semilog scale; the simulation time is extended in order to capture the long term behavior of h_{end}. Unsurprisingly, the faster the speed of the moving end, the smaller h_{min}, for all time points, and for both moderate and weak elasticity models. Comparing the minimum thickness in Figs. 14 and 15, the trend over time is remarkably similar, although h_{min} is slightly lower for the case of moderate elasticity. When $v_0 = 2.5$, the sheet

reaches the minimum threshold thickness of $h = 0.01$ between $t = 6$ and $t = 7$, in the case of both weak and moderate elasticity. We note that in the case of moderate elasticity, as time progresses, the plots of h_{end} vs time for different v_0-values exhibit several crossings, starting around $t = 4$. This contrasts with the case of weak elasticity shown in Fig. 15, where the value of h_{end} is always monotone decreasing as v_0 increases for all times in the simulation interval. This is another way in which the model with moderate elasticity differs from that with weak elasticity.

The moderate elasticity solutions for the sheet thickness, axial velocity, and pressure corresponding to Fig. 14 with $v_0 = 2$ are shown in Fig. 16. While the initial sheet profile is retained, qualitatively, under stretching, the right end is slightly thinner than the left. The slower the speed of the moving end, the more of the original wave is lost as time progresses.

Figure 17 compares sheet evolution in time, for the moderate and weak elasticity cases, for three different values of the sheet extension speed v_0 at times $t = 0.5$ and $t = 4$. At all speeds, the sheet with weak elasticity remains symmetric about its midpoint, and retains the wavenumber of the initial condition while being stretched over the increasing domain. This is not the case for moderate elasticity solutions. For the slowest extension speed $v_0 = 0.5$, the moving end of the sheet thins significantly, such that roughly half of the initial wave is lost by $t = 0.5$, leading to very large differences between the weak and moderate elasticity predictions. When $v_0 = 1$, more of the original shape is retained, but the moving end still thins significantly relative to the left end; the prediction is again substantially different from the weak
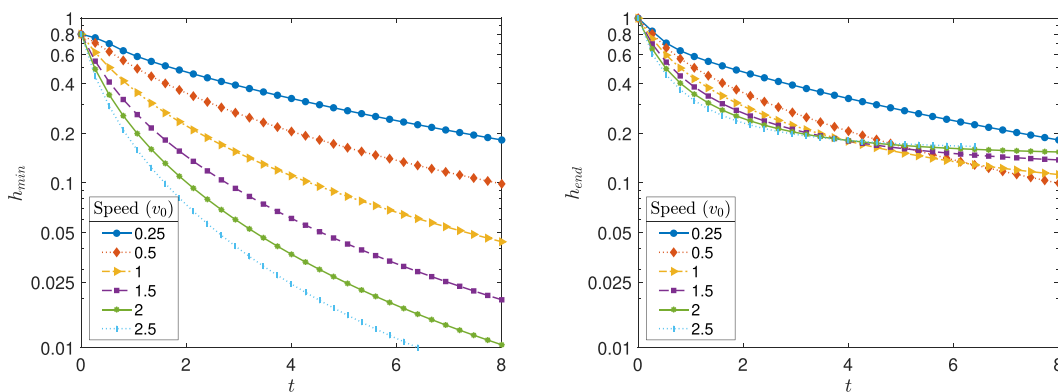

FIG. 14. Evolution of h_{min} and h_{end} for moderate elasticity as the speed varies from 0.25 to 2.5. Results are for BC case I with $S = 0.025$.
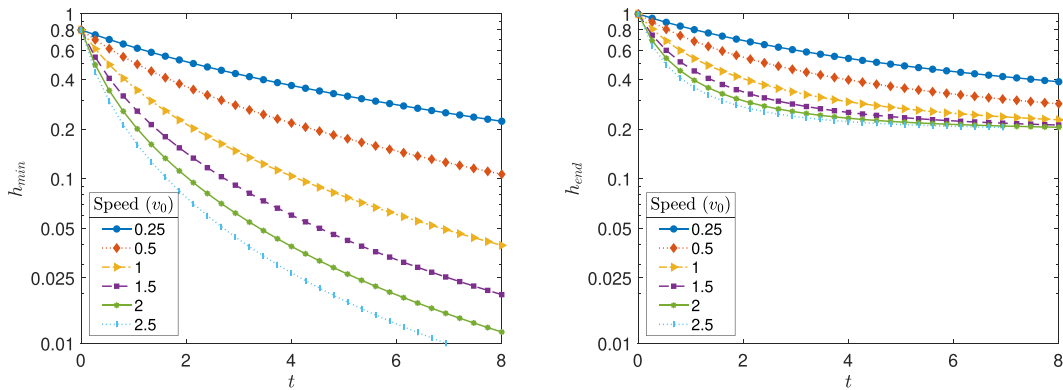
FIG. 15. Evolution of $h_{\min}$ and h_{end} for weak elasticity as the speed varies from 0.25 to 2.5. Results are for BC case I with $S = 0.025$.
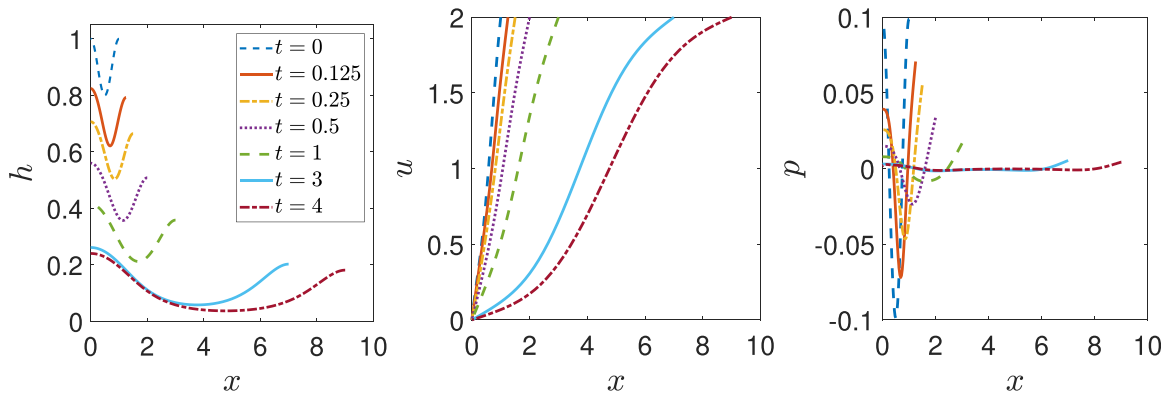

FIG. 16. Solutions for sheet thickness, h, fluid velocity, u, and pressure, p, for moderate elasticity. Results are for BC case I with $S = 0.025$, and $v_0 = 2$.

elasticity case. The differences between the two models are least pronounced for the fastest extension speed $v_0 = 2$. At both time points shown, the moderate elasticity model yields a sheet that is only slightly thicker over the left half than the right. The sheet thickness at the left end remains very similar for the two models, but the moving end of the sheet with moderate elasticity is thinner.

F. Increasing wavenumber in ICs

Imaging of the tear film has on occasion shown stripes or ridges in the lipid layer.[1] To investigate whether our model can sustain multiple waves during extensional flow, we experiment with increasing the wavenumber k_0 in the initial condition Eq. (21). For all of the following results, we use the case of moderate elasticity with BC case I and $v_0 = 1$.

Figure 18 shows the sheet solution profiles at $t = 0.5$ and $t = 3$ for three different values of the initial wavenumber k_0. For each IC, the sheet thickness is shown for three different values of the surface tension number, $S = 0.0025$, 0.01, and 0.025. The lower the surface tension, the more of the original waves are retained as time progresses. We note that the reduction of wavenumber appears to be complete by time $t = 0.5$; after that, the resulting shape primarily stretches as the

sheet lengthens (this point is discussed further below). In particular, in the first example with wavenumber $k_0 = 2$, both waves are retained for the smallest value of S, while for $S = 0.01$ and $S = 0.025$, half a wave and a full wave (respectively) are lost from the initial shape by the final time. Similar differences are also apparent at higher wavenumbers: for $k_0 = 2.5$ the smallest surface tension simulation ($S = 0.0025$) loses just half a wave by the final time, while $S = 0.01$ loses a full wave and $S = 0.025$ loses 1.5 waves; and for $k_0 = 3$ the simulation for $S = 0.0025$ again loses just half a wave, while $S = 0.01$ loses 1.5 waves and $S = 0.025$ loses 2 full waves.

We further investigate simulations for $S = 0.0025$, since this value leads to persistent waves in the sheet. For this value of S we vary the wave amplitude b in the initial condition Eq. (21) and observe the change of wavenumber over time as the sheet is stretched (specifically, the number of complete waves that are lost); the results are summarized in Table IV. The top row of this table corresponds to the $S = 0.0025$ simulations of Fig. 18. We see that the value of the initial wavenumber k_0 is more influential than the initial wave amplitude b.

We also test our earlier assertion, that the reduction in wavenumber appears to be determined at an early stage of the stretching, by running simulations to larger times. We used the event detection option in MATLAB and let the sheet stretch until $h_{\min} < 0.01$ (assumed
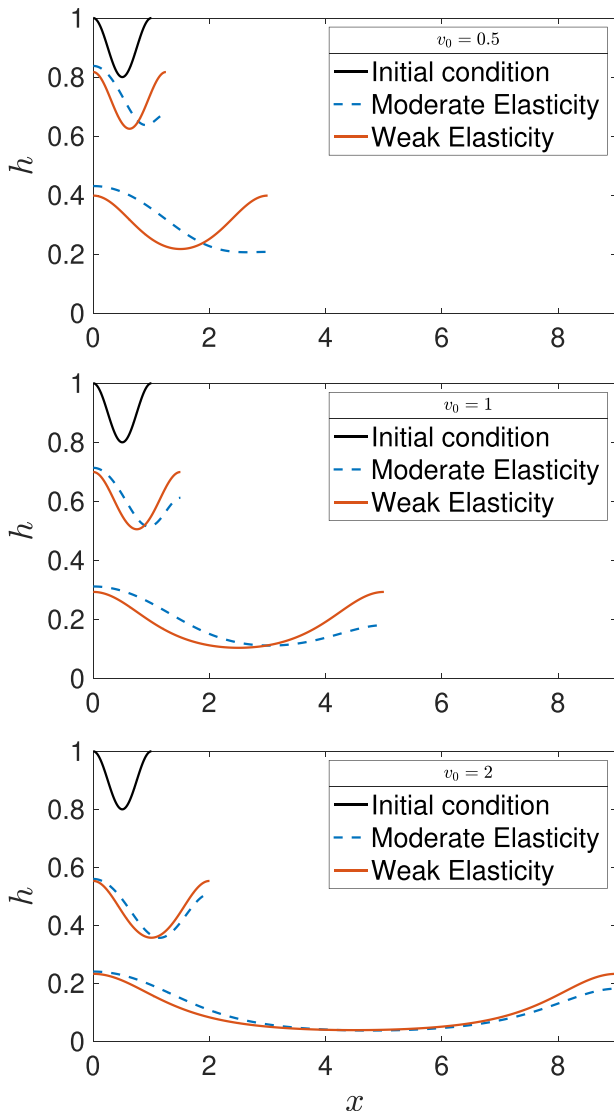
FIG. 17. Sheet thicknesses for moderate and weak elasticity models for increasing values of extension speed v_0, shown at times $t = 0.5$ and $t = 4$. The solid black curve shows the initial sheet profile for both models at $t = 0$. Results are shown for BC case I, with $S = S_w = 0.025$.

to represent sheet breakup in the model). The results are summarized in Table V, which records the IC used in the simulation, the time to breakup, the number of waves lost from the IC during evolution, and whether the final extremum of sheet thickness at the moving end is a maximum or minimum. In each case, the sheet reached this minimum thickness threshold before any noticeable change in shape from that noted at $t = 0.5$. When the moving end of the sheet is (or evolves to) a local minimum, the sheet "breaks" faster than when the moving end is a local maximum (sheet contains an integer number of full waves). For example, the two ICs with $k_0 = 2.5$ and $k_0 = 3$ both lose half a wave under stretching. The curve resulting from $k_0 = 2.5$ develops a local maximum at the right end, and can stretch for more than twice
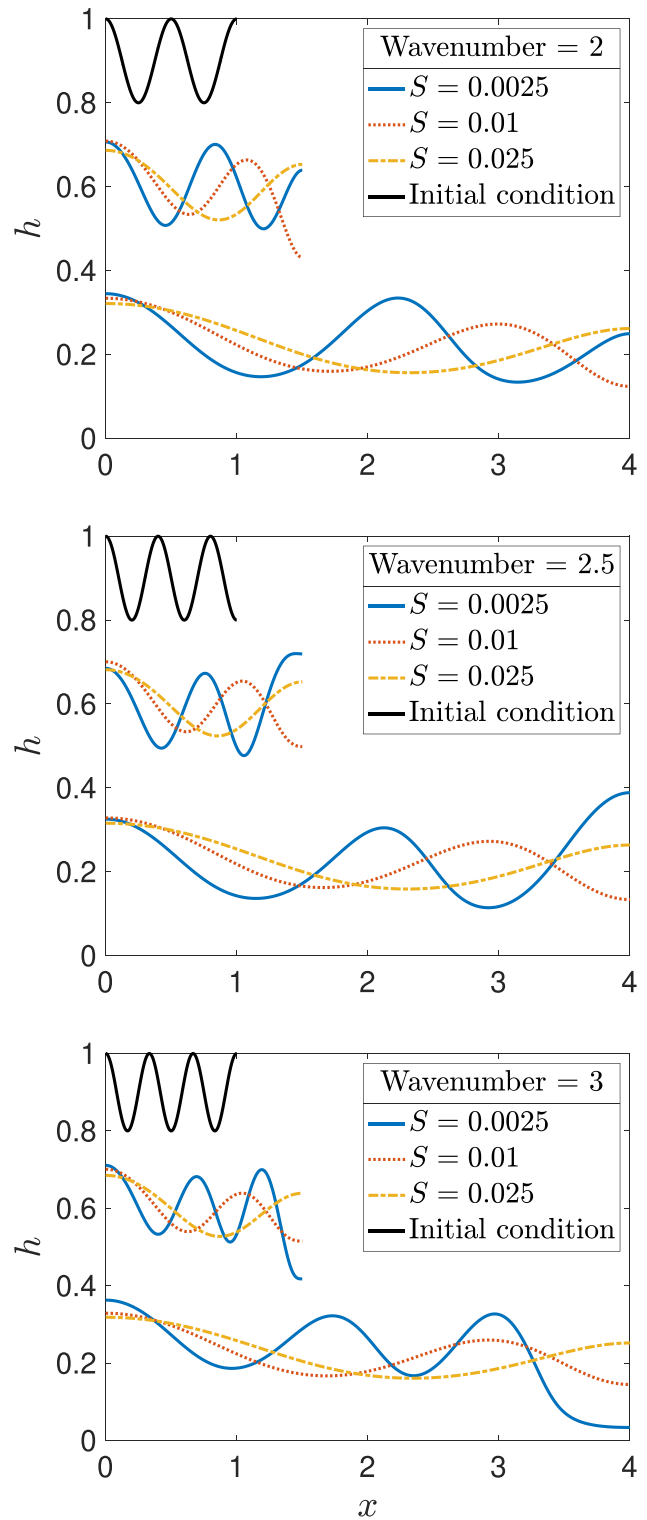

FIG. 18. Profiles of sheet thickness, h, at $t = 0$ (top curve in each plot), $t = 0.5$ (middle curves), and $t = 3$ (bottom curves) when the initial condition Eq. (21) has wavenumber $k_0 = 2$, 2.5, and 3 ($b = 0.1$, $a = 0.9$ in all cases).

16 October 2023 13:11:32

TABLE IV. Table entries show number of waves lost from initial condition Eq. (21) at $t = 4$ as amplitude b and wavenumber k_0 are varied. Here, $a = 1 - b$ in Eq. (21) and $S = 0.0025$.

Amplitude b	Wavenumber k_0						
	1	1.5	2	2.5	3	3.5	4
0.2	0	0	0	1/2	1/2	$\cdots$	$\cdots$
0.1	0	0	0	1/2	1/2	1	1
0.05	0	0	0	1/2	1/2	1	1
0.025	0	0	0	1/2	1/2	1	1

TABLE V. Comparison of the time to reach $h = 0.01$, which represents sheet breakup, for various initial conditions when $S = 0.0025$. Here $a = 0.9$ and $b = 0.1$.

Initial condition	Time to $h < 0.01$	Waves lost	Final extremum at right
$a + b\cos(3\pi x)$	12.9935	None	Minimum
$a + b\cos(4\pi x)$	13.4664	None	Maximum
$a + b\cos(5\pi x)$	10.2892	1/2	Maximum
$a + b\cos(6\pi x)$	4.2099	1/2	Minimum
$a + b/2\cos(5\pi x)$	18.2691	1/2	Maximum
$a + b/2\cos(6\pi x)$	9.5259	1/2	Minimum

as long as the $k_0 = 3$ simulation, which develops a local minimum there. Figure 19 shows the sheet profiles at the time that the thickness reaches the threshold of $h = 0.01$ for four initial conditions. Interestingly, although the sheet profiles that have a minimum at the moving end always appear to break first, the breakup does not always appear at the moving end, but may happen at an interior minimum.

G. Increasing wavenumber in IC with Robin BCs

We now turn to BC case V and vary the initial shape of the film for $S = 0.0025$. Computed results are shown in Fig. 20 for wavenumbers $k = 0$ (initially flat), 1, 2, and 3. For $k = 0$ (upper left), the film quickly develops thickness variation with menisci at the ends and two internal maxima. As the film stretches, it thins between the left (fixed) end and the closest maximum, developing a fairly wide thin region on the left with more fluid gathering toward the moving end. This dynamic is much like that in Fig. 11. The two internal maxima persist throughout the computed interval, though they both become less pronounced as time progresses.

With $k = 1$ (upper right), a single internal maximum is generated. Between the fixed end and this maximum there is thinning, but it is much less pronounced than for $k = 0$. For $k = 2$, a second internal maximum is generated near the fixed end, and persists thoughout the computed interval. The maximum is pulled away from the left end, but once again the thinning is less pronounced than for $k = 0$ or for Fig. 11.

For $k = 3$, the dynamics are more complex. An internal maximum is generated near the left end again, and it persists throughout the computation. At the right end, the internal maximum nearest the moving end is lost sometime shortly after $t = 1$, and the relative size of the end point and the closest interior maximum changes during $0 < t < 1$. By $t = 4$, there are just two internal maxima again and they are less pronounced as the film stretches.

These results suggest that the Robin condition (close to Dirichlet) at the fixed end can generate waves, and that waves can be lost at the moving end. In either case, a thin area near the end can be generated.
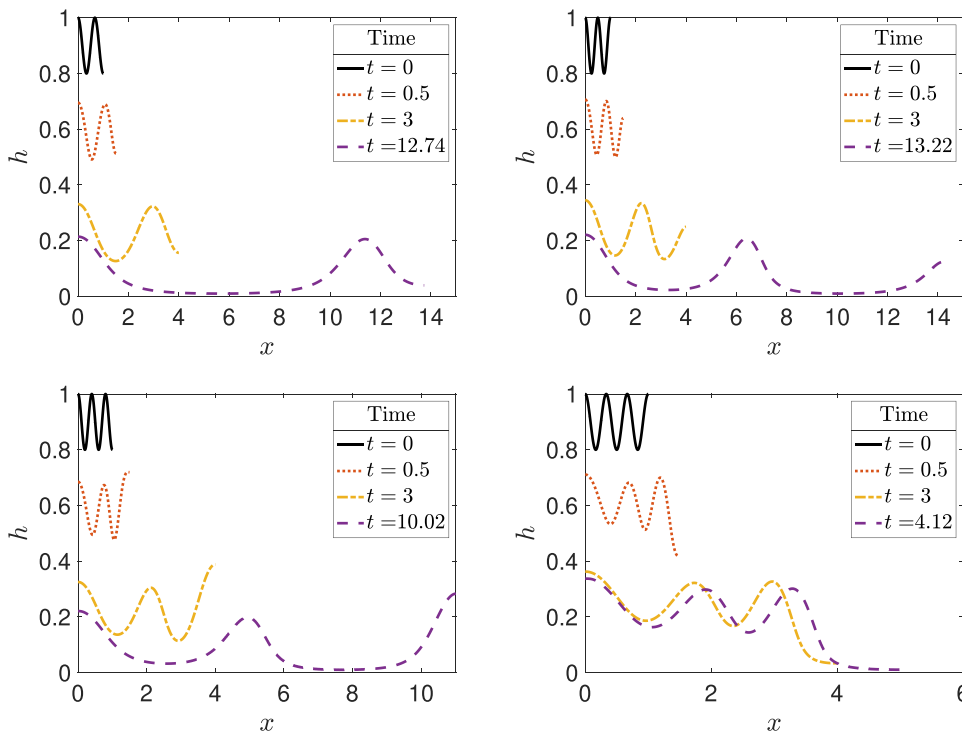

FIG. 19. Sheet thickness, h, at $t = 0$ (top curve in each plot), $t = 0.5$ (second curve), and $t = 3$ (third curve) and the time to reach the threshold thickness of $h = 0.01$ (bottom curve) for initial condition Eq. (21) with $a = 0.9$, $b = 0.1$ and wavenumbers $k_0 = 1.5$, 2, 2.5, and 3 with $v_0 = 1$.
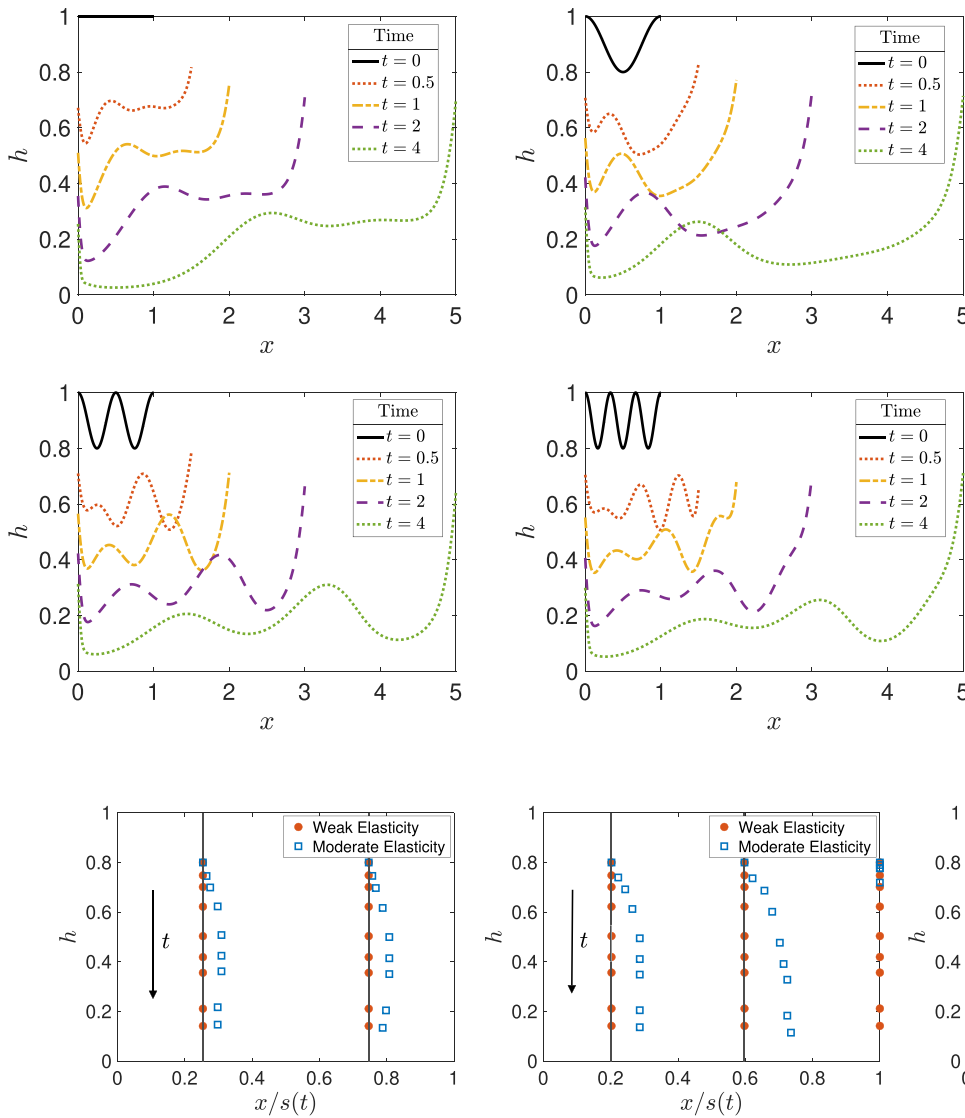
FIG. 20. Sheet thickness, h, at $t = 0$, 0.5, 1, 2, 4 for initial condition Eq. (21) with $a = 0.9, b = 0.1$ and wavenumbers $k_0 = 0$, 1, 2, and 3 with $v_0 = 1$ and $S = 0.0025$.

FIG. 21. Location of local minima in thickness, for weak and moderate elasticity models, at $t = 0$, 0.0625, 0.125, 0.25, 0.5, 0.75, 1, 2, 3 on a fixed domain with $S = S_w = 0.0025$, $v_0 = 1$. From left to right, each plot corresponds to a different wavenumber: $k_0 = 2$, 2.5, 3 in Eq. (21) (with $a = 0.9, b = 0.1$). The straight black lines emphasize that locations of thickness minima are stationary for weak elasticity on a fixed domain.
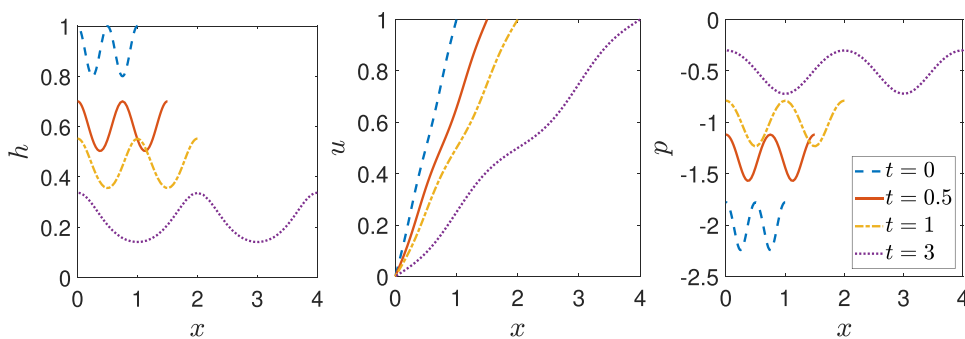

FIG. 22. Profiles of sheet thickness, h, fluid velocity, u, and pressure, p, for the case of weak elasticity when $k_0 = 2$. Results are for BC case I with $S = 0.0025$ and $v_0 = 1$.
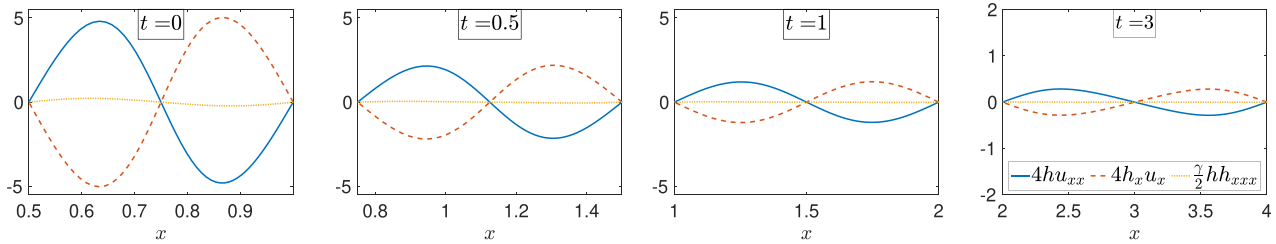
FIG. 23. Individual terms in the axial force balance Eq. (5) for the case of weak elasticity shown in Fig. 22 ($k_0 = 2$). Note that only the right half of the domain is shown, and the scale of the vertical axis changes in the final plot.

H. Mechanisms

For weak elasticity, the oscillations contained in the initial condition are retained in the sheet throughout time, and are stretched as the sheet lengthens. The sheet retains any symmetry in the initial condition, and the locations of minimum and maximum thicknesses are unchanged through time when plotted in terms of the coordinate $\xi = x/s(t)$; see Fig. 21. The solutions for sheet thickness, velocity, and pressure when the initial condition contains 2 waves ($k_0 = 2$) are shown in Fig. 22. If we compare the individual terms of the PDE, as shown in Fig. 23 (where only the right half of the domain is shown), we see that it is primarily the extensional terms from $(h u_x)_x$ that balance; the role of surface tension is minor. The velocity profile is nearly linear with small fluctuations in the slope. Pressure remains negative through the entire sheet, as extension is dominating capillarity, and decreases in magnitude as the sheet lengthens.

However, for moderate elasticity, solutions are more complicated. We compare the sheet thickness, velocity, and pressure when the initial condition contains either two and a half ($k_0 = 2.5$) or three ($k_0 = 3$) waves; the solutions are shown in Figs. 24–26. When $k_0 = 2.5$ (Fig. 24), the moving end begins as a thickness minimum. Local low pressure draws fluid toward the moving end, and this local minimum becomes a global maximum by time $t = 0.5$. The minimum thickness occurs in the interior, in the trough closest to the moving end. The early rapid movement of fluid toward the moving end is shown in the velocity profile at $t = 0.0625$, where the velocity briefly increases above the pulling velocity ($v_0 = 1$) near the moving end. Fluctuations in the velocity profile smooth after this time, and the profile becomes nearly linear. Pressure decays to near zero for $t > 1$. Figure 25 shows the role of each term in the PDE. At early times, we see that the terms with the highest derivatives are flipping roles. As pressure diminishes, extensional terms take over.

When $k_0 = 3$ (Fig. 26), we see the role of pressure has changed. Together, pressure and extension prevent fluid from keeping up with the moving end, and the right end quickly becomes the global minimum. A boundary layer in the velocity profile is seen to form at the right end of the sheet in the middle column of Fig. 26. A maximum in the pressure develops at the right end by $t = 0.0625$, and remains a global maximum until about $t = 0.25$. The pressure diminishes thereafter.

In summary, our results for the moderate elasticity model show that, depending on the initial condition and boundary conditions, the number of waves in the sheet is typically reduced, and there are significant changes in the shape of the sheet as fluid moves due to changes in pressure. An exception was for BC case V in Fig. 20 with $k_0 = 2$ where additional maxima appeared inside the domain. Model parameters, in

particular the surface tension number S, can also strongly influence the number of waves retained in the sheet under extension; in this subsection such model parameters were fixed. At early times, pressure either cooperates with or opposes extension at the moving end, which redistributes fluid there and may result in the loss of a maximum or minimum in the sheet thickness there. When a maximum is lost from the moving end, a boundary layer forms in the velocity profile. As time increases, the pressure decreases in magnitude, its influence on the shape of the sheet decreases, and the role of the extension becomes
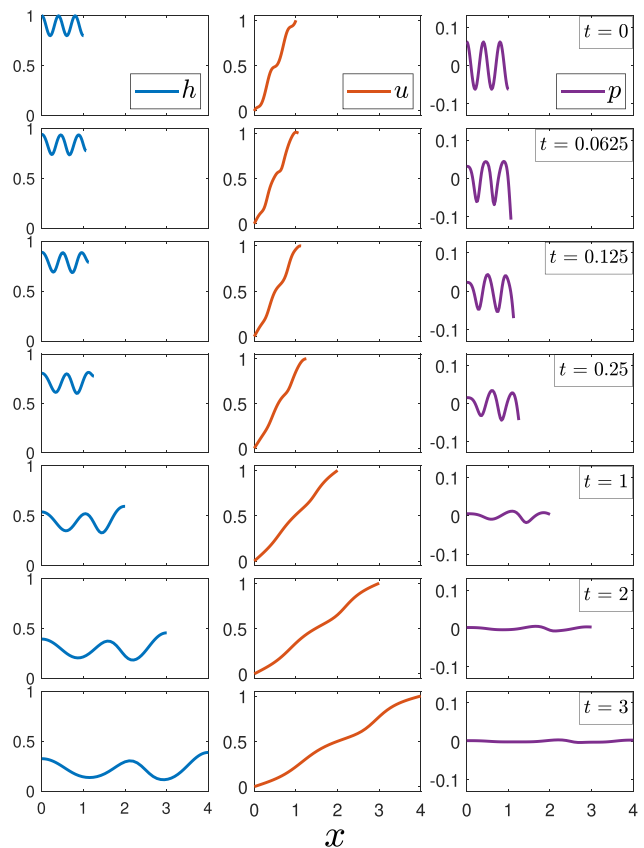

FIG. 24. Sheet thickness, h, fluid velocity, u, and pressure, p, for the case of moderate elasticity when the initial condition has two and a half waves ($k_0 = 2.5$). Results are for BC case I with $S = 0.0025$ and $v_0 = 1$. Each row represents a time level; each column shows the respective dependent variable.
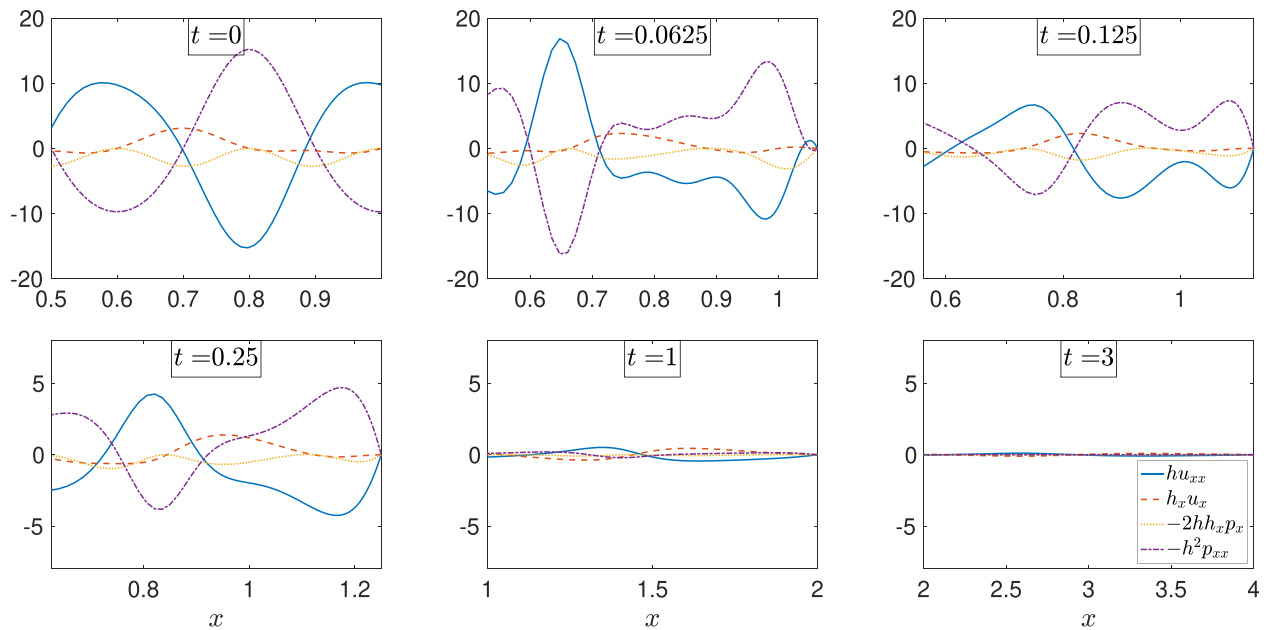
FIG. 25. Individual terms in the axial force balance Eq. (18) for the case of moderate elasticity whose full profiles are shown in the previous Fig. 24 ($k_0 = 2.5$); only half the domain is shown here. Note that the scale of the vertical axis changes on the second row.

more pronounced. In general, the roles of pressure and extension are more intertwined than in the case of weak elasticity.

V. DISCUSSION AND CONCLUSION

We present a new model for describing the extensional 2D flow of nematic liquid crystal sheets with moderate elasticity, and compare results to the analogous weak elasticity model. For moderate elasticity, the pressure, surface tension and elastic energy were all promoted to larger values compared to the weak elasticity case studied by Cummings et al.[43] The axial force balance, Eq. (14), in the new model is of higher spatial order than the model for weak elasticity; in terms of the sheet thickness, the equation is fourth order rather than third in spatial derivatives. This change necessitates an additional boundary condition. Consideration of the individual terms in the sheet tension in Eq. (20) motivated the additional condition that we used, $p_x(0, t) = 0$. Numerical exploration suggested that the single equation Eq. (16), describing the sheet profile evolution, may be viewed as being dispersive, and that the additional boundary condition may be considered as specifying the value for an incoming characteristic.

For initial conditions, we use sinusoidal curves, and we explore a range of initial wavenumbers. Further work could include formulating a consistent initial condition for a Dirichlet condition on either end. We examine the effect of varying surface tension and the speed of the moving end on the dynamics of the evolving sheet under stretching.

The response of the moderately elastic sheet is markedly different from that of weak elasticity or Newtonian fluids. Cummings et al.[43] modeled liquid crystal sheets with weak elasticity, however that work focused primarily on the effect of an electric field on the liquid crystal. For liquid crystals with moderate elasticity, the elastic quality of the material is demonstrated well in Fig. 21, which shows a recoil in the location of minima in a sheet with multiple waves. In the case of weak

elasticity, the minima maintain their relative position in the sheet while undergoing stretching. In Fig. 12, we show that, depending on the initial condition, the minimum sheet thickness can occur at almost any position in the sheet, from the very right end, to close to the left end. When varying the surface tension, we again see the elastic quality of the material; see Fig. 13. When varying the speed of the moving end, we see that for the same speed, the sheet with moderate elasticity thins slightly faster than in the case of weak elasticity; see Fig. 14.

We also considered dynamics for different initial wavenumbers in the sheet profile. We increase the number of waves in the initial condition, and observe the shape of the sheet as it undergoes stretching. We find, as might be expected, that the higher the surface tension, the more waves are lost from the initial shape under stretching. The amplitude of the waves has much less influence than the number of waves, as seen in Table IV. At early times, depending on the number of sinusoidal waves in the initial condition, pressure either aids or opposes extensional flow, which changes the shape of the sheet and may result in the loss of a minimum or maximum at the moving end. When a maximum is lost from the moving end, and specifically when the moving end switches from a maximum to a minimum, we see a boundary layer form in the velocity profile. Fluid flows quickly out of the region at the end, and the sheet is unable to stretch for very long times before numerics fail. This illustrates the more prominent role that pressure plays in determining the shape of the sheet with moderate elasticity; see, for example, Fig. 25.

The menisci that develop in the thickness profiles when using Robin boundary conditions for moderate elasticity are reminiscent of the profiles found by several previous authors[54–61] for the aqueous layer of the tear film during a blink. Specifically, BC case III (Robin condition at the moving end) yields profiles comparable to those of the tear film during the upstroke of a blink. BC case IV (Robin
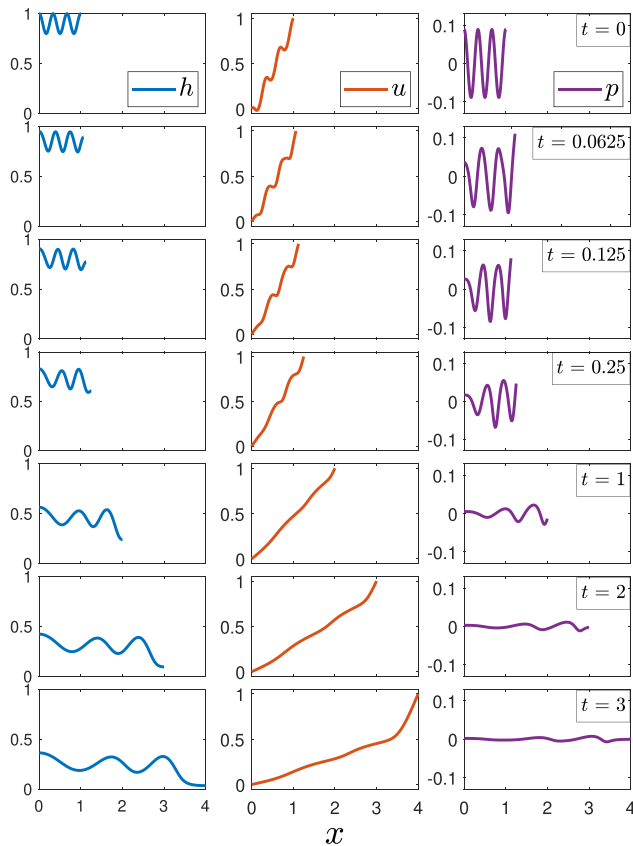
FIG. 26. Profiles of sheet thickness, h, fluid velocity, u, and pressure, p, for the case of moderate elasticity when the initial condition has three waves ($k_0 = 3$) and $S = 0.0025$. Each row represents a time level; each column shows the dynamics of the respective dependent variable.

condition at the fixed end) is similar to the meniscus corresponding to the lower lid during the upstroke when the upper lid would be moving away from it.

We note that weak and moderate elasticity limits were considered for a nematic liquid crystal film on a substrate by Lin *et al.*[44] Those authors found that a larger scaling for the elastic terms (only) introduced an additional term in the single nonlinear PDE for the thickness h; the new term was diffusion-like and is similar to the effect of gravity in Newtonian films.[62] In our work, there is no substrate for the free film, and compared to the weakly elastic limit, we made both the elastic and surface tension parameters larger. As a result, we scaled the pressure to be larger, and the new balance gave us two PDEs, one each for the film thickness h and axial velocity u, as is typical for extensional flow.[43] The results reported here clearly show elastic behavior, and likely more obviously than the model found by Lin *et al.*[44]

There are some limitations with our model in terms of computing for a longer time interval for a wider range of parameter values. Both the finite differences and spectral methods work well up until $t = 3$, and for some parameter values, much longer than that; however, to run other cases for longer time may require domain decomposition or an adaptive method to adequately resolve regions of small thickness.[63] Scenarios that result in beads on a string[40,41] involve much more

extension and longer computation times than we studied; it is unclear what patterns would result if we were to apply more complicated numerical methods to long times in our setting.

We shall continue developing more physiologically relevant models for the lipid layer of the tear film in the eye. This will require using more realistic parameter values, and modifying the sheet's end speed to be more realistic.[32,33,56,59] We have a model in hand with a shear-dominated aqueous layer added to the lipid layer in the spirit of previous works.[52,64–66] Much work remains to connect the dynamics of such models to the observed patterns of the lipid layer in the tear film.

ACKNOWLEDGMENTS

AUTHOR DECLARATIONS
Conflict of Interest

The authors have no conflicts to disclose.

Author Contributions

Mary J. Taranchuk: Formal analysis (lead); Writing – original draft (equal); Writing – review & editing (equal). **Linda J. Cummings:** Formal analysis (equal); Funding acquisition (equal); Supervision (equal); Writing – original draft (equal); Writing – review & editing (equal). **Tobin A. Driscoll:** Formal analysis (equal); Funding acquisition (equal); Supervision (supporting); Writing – original draft (supporting); Writing – review & editing (equal). **Richard J. Braun:** Conceptualization (lead); Formal analysis (equal); Funding acquisition (equal); Project administration (lead); Supervision (equal); Writing – original draft (equal); Writing – review & editing (equal).

DATA AVAILABILITY

Data sharing is not applicable to this article as no new data were created or analyzed in this study.

APPENDIX A: DERIVATIONS

1. Ericksen–Leslie equations

The Ericksen–Leslie equations describe the flow of nematic liquid crystals, and are based on principles of conservation of mass, momentum and energy. In dimensional form, with a prime denoting a dimensional quantity,

$$\frac{\partial}{\partial x'}\left(\frac{\partial W'}{\partial \theta_x}\right) + \frac{\partial}{\partial z'}\left(\frac{\partial W'}{\partial \theta_z}\right) - \frac{\partial W'}{\partial \theta} + \tilde{g}'_x \frac{\partial n_x}{\partial \theta} + \tilde{g}'_z \frac{\partial n_z}{\partial \theta} = 0, \quad \text{(A1)}$$

$$-\frac{\partial \pi'}{\partial x'} + \tilde{g}'_x \frac{\partial n_x}{\partial x'} + \tilde{g}'_z \frac{\partial n_z}{\partial x'} + \frac{\partial \sigma^{V'}_{xz}}{\partial z'} + \frac{\partial \sigma^{V'}_{xx}}{\partial x'} = 0, \quad \text{(A2)}$$

$$-\frac{\partial \pi'}{\partial z'} + \tilde{g}'_x \frac{\partial n_x}{\partial z'} + \tilde{g}'_z \frac{\partial n_z}{\partial z'} + \frac{\partial \sigma^{V'}_{zx}}{\partial x'} + \frac{\partial \sigma^{V'}_{zz}}{\partial z'} = 0, \quad \text{(A3)}$$

$$\frac{\partial v'}{\partial x'} + \frac{\partial w'}{\partial z'} = 0, \quad \text{(A4)}$$

where

$$\tilde{g}'_i = -\gamma_1 N'_i - \gamma_2 e'_{ik} n_k, \quad e'_{ij} = \frac{1}{2}\left(\frac{\partial v'_i}{\partial x'_j} + \frac{\partial v'_j}{\partial x'_i}\right), \quad \text{(A5)}$$

$$N'_i = \frac{Dn'_i}{Dt} - \omega'_{ik} n_k, \quad \omega'_{ij} = \frac{1}{2}\left(\frac{\partial v'_i}{\partial x'_j} - \frac{\partial v'_j}{\partial x'_i}\right), \quad \pi' = p' + W', \quad \text{(A6)}$$

$$W' = \frac{1}{2}\left[K_1(\nabla' \cdot \mathbf{n})^2 + K_2(\mathbf{n} \cdot \nabla' \wedge \mathbf{n})^2 + K_3((\mathbf{n} \cdot \nabla')\mathbf{n}) \cdot ((\mathbf{n} \cdot \nabla')\mathbf{n})\right], \quad \text{(A7)}$$

$$\sigma^{V'}_{ij} = \alpha'_1 n_k n_p e'_{kp} n_i n_j + \alpha'_2 N'_i n_j + \alpha'_3 N'_j n_i + \alpha'_4 e'_{ij} + \alpha'_5 e'_{ik} n_k n_j$$
$$+ \alpha'_6 e'_{jk} n_k n_i, \quad \text{(A8)}$$

$$\sigma^{E'} = W'_{\nabla \mathbf{n}} \cdot (\nabla \mathbf{n})^T, \quad \text{(A9)}$$

$$\sigma' = -p'\mathbf{I} + \sigma^{E'} + \sigma^{V'}. \quad \text{(A10)}$$

Here **I** is the identity tensor, summation over the repeated indices is understood, and $\frac{D}{Dt} = \partial/\partial t + \mathbf{v} \cdot \nabla$ denotes the convective derivative. We use bold font for vectors relating to the liquid crystal, while italics are used for the normal and tangent vectors on the surface, as seen in the following paragraphs. We take $K = K_1 = K_2 = K_3$ to be the one-constant approximation to the elastic constants, with K_1 being the single value used.[43,47] The quantities defined above are described in Table VI. In two dimensions, the energy and the stress tensor then simplify to

$$W' = \frac{K}{2}(\theta^2_{x'} + \theta^2_{z'}), \quad \text{(A11)}$$

TABLE VI. Parameters and variables used in the model.[47]

Quantity	Description
$\mathbf{v}' = (u', w')$	Velocity field of the flow
$\mathbf{n} = (\sin\theta, \cos\theta)$	Director field
$\theta(x, z, t)$	Angle the director angle makes with the z-axis
p'	Pressure
W'	Bulk energy density
$\pi' = p' + W'$	Modified pressure
$\sigma^{V'}_{ij}$	Viscous stress tensor
$\sigma^{E'}_{ij}$	Elastic stress tensor
σ'	Stress tensor
$\alpha'_i, i = 1, \dots, 6$	Leslie viscosities (Newtonian: $\mu' = \alpha'_4/2$, all other $\alpha_i = 0$)
$\gamma'_1 = \alpha'_3 - \alpha'_2$	Rotational/twist viscosity
$\gamma'_2 = \alpha'_6 - \alpha'_5$	Torsion coefficient
K_1, K_2, K_3	Elastic constants representing splay, twist, and bend respectively
ω'_{ij}	Vorticity tensor
e'_{ij}	Rate of strain tensor
N_i	Co-rotational time flux of the director **n**

$$\sigma' = -p'\begin{bmatrix} 1 & 0 \\ 0 & 1 \end{bmatrix} - K\begin{bmatrix} \theta^2_{x'} & \theta_{x'}\theta_{z'} \\ \theta^2_{z'} & \theta_{x'}\theta_{z'} \end{bmatrix} + \begin{bmatrix} \sigma^{V'}_{11} & \sigma^{V'}_{12} \\ \sigma^{V'}_{21} & \sigma^{V'}_{22} \end{bmatrix}. \quad \text{(A12)}$$

The fully expanded version of σ' is very lengthy; for an explicit presentation, see Lin *et al.*[44]

We solve the governing equations subject to the boundary conditions that follow. We list the boundary conditions for the top surface, $z' = \frac{1}{2}h'(x', t')$ only; those for the bottom surface, $z' = -\frac{1}{2}h'(x', t')$, are defined analogously. The normal stress condition is

$$\hat{n}' \cdot \sigma' \cdot \hat{n}' = -\gamma' \kappa' \hat{n}' \quad \text{at} \quad z = \frac{1}{2}h'(x', t'), \quad \text{(A13)}$$

where $\hat{n}' = (-h'_{x'}/2, 1)/\sqrt{1 + (h'_{x'}/2)^2}$ is the unit vector normal to the top surface, and $\kappa' = -\nabla \cdot \hat{n}'$ is the curvature of the top surface. The definition of σ' is taken from Lin *et al.*,[44] and contains an additional term from the form given in Cummings *et al.*[43] The tangential stress condition is

$$\hat{n}' \cdot \sigma' \cdot \hat{t}' = 0 \quad \text{at} \quad z' = \frac{1}{2}h'(x', t'), \quad \text{(A14)}$$

where $\hat{t}' = (1, h'_{x'}/2)/\sqrt{1 + (h'_{x'}/2)^2}$ is the unit vector tangent to the top surface. The kinematic boundary condition is

$$w' = \frac{1}{2}\left(h'_{t'} + u'h'_{x'}\right) \quad \text{at} \quad z' = \frac{1}{2}h'(x', t'). \quad \text{(A15)}$$

Finally, the anchoring boundary condition is

$$\theta = \theta_B \quad \text{at} \quad z' = \frac{1}{2}h'(x', t'). \quad \text{(A16)}$$

2. Scalings for weak elasticity

The scalings for weak elasticity are as in Eqs. (1) and (2), along with

$$\hat{N}_w = \frac{K}{\mu \hat{U} \delta L}, \quad W' = \frac{K}{\delta^2 L^2}W, \quad \alpha'_i = \mu \alpha_i.$$

Nondimensionalizing with these scalings yields

$$\hat{N}\frac{\partial}{\partial x}\left(\frac{\partial W}{\partial \theta_x}\right) + \hat{N}\frac{\partial}{\partial z}\left(\frac{\partial W}{\partial \theta_z}\right) - \hat{N}\frac{\partial W}{\partial \theta} + g_x\frac{\partial n_x}{\partial \theta} + g_z\frac{\partial n_z}{\partial \theta} = 0, \quad \text{(A17)}$$

$$-\delta^2\frac{\partial p}{\partial x} - \delta\hat{N}\frac{\partial W}{\partial x} + \delta g_x\frac{\partial n_x}{\partial x} + \delta g_z\frac{\partial n_z}{\partial x} + \delta\frac{\partial \sigma^V_{xx}}{\partial x} + \frac{\partial \sigma^V_{xz}}{\partial z} = 0, \quad \text{(A18)}$$

$$-\delta\frac{\partial p}{\partial z} - \hat{N}\frac{\partial W}{\partial z} + g_x\frac{\partial n_x}{\partial z} + g_z\frac{\partial n_z}{\partial z} + \delta\frac{\partial \sigma^V_{zx}}{\partial x} + \frac{\partial \sigma^V_{zz}}{\partial z} = 0. \quad \text{(A19)}$$

Then, the leading order system of equations is

$$h_t + (hu)_x = 0, \quad \text{(A20)}$$

$$\frac{F(\theta_B)}{G(\theta_B)}(hu_x)_x + \frac{S_w}{2}hh_{xxx} = 0, \quad \text{(A21)}$$

where

$$G(\theta_B) = \alpha_1 - 2\alpha_2 + 2\alpha_3 + 8 + 2\alpha_5 + 2\alpha_6 - \alpha_1 \cos(4\theta_B)$$
$$-2\cos(2\theta_B)(\alpha_2 + \alpha_3 - \alpha_5 + \alpha_6), \tag{A22}$$

$$F(\theta_B) = \alpha_1(-\alpha_2 + \alpha_3 + 8 + 2\alpha_5 + 2\alpha_6) - \alpha_2(8 + \alpha_5 + 3\alpha_6)$$
$$+\alpha_3(8 + \alpha_5 + \alpha_6) + 32 + \alpha_5(16 + 2\alpha_5 + 4\alpha_6) + \alpha_6(16 + 2\alpha_6)$$
$$-2\cos(2\theta_B)(\alpha_1 + 4 + \alpha_5 + \alpha_6)(\alpha_2 + \alpha_3 - \alpha_5 + \alpha_6)$$
$$-\cos(4\theta_B)[\alpha_1\alpha_2 - \alpha_1\alpha_3 + (\alpha_2 + \alpha_3)(\alpha_5 - \alpha_6)]. \tag{A23}$$

In the Newtonian case, viscosities $\alpha_i = 0$, $(i = 1, 2, 3, 5, 6)$, and $F(\theta_B)/G(\theta_B) = 4$.

3. Deriving the equations for moderate elasticity

To consider the case of moderate elasticity, we rescale the inverse Ericksen number, the pressure, and the surface tension number as in Eq. (11), while keeping the other scalings the same. Then, the nondimensionalized governing equations become

$$\hat{N}\frac{\partial}{\partial x}\left(\frac{\partial W}{\partial \theta_x}\right) + \hat{N}\frac{\partial}{\partial z}\left(\frac{\partial W}{\partial \theta_z}\right) - \hat{N}\frac{\partial W}{\partial \theta} + \delta g_x \frac{\partial n_x}{\partial \theta} + \delta g_z \frac{\partial n_z}{\partial \theta} = 0, \tag{A24}$$

$$-\delta \frac{\partial p}{\partial x} - \hat{N}\frac{\partial W}{\partial x} + \delta g_x \frac{\partial n_x}{\partial x} + \delta g_z \frac{\partial n_z}{\partial x} + \delta \frac{\partial \sigma^V_{xx}}{\partial x} + \frac{\partial \sigma^V_{xz}}{\partial z} = 0, \tag{A25}$$

$$-\delta \frac{\partial p}{\partial z} - \hat{N}\frac{\partial W}{\partial z} + \delta g_x \frac{\partial n_x}{\partial z} + \delta g_z \frac{\partial n_z}{\partial z} + \delta^2 \frac{\partial \sigma^V_{zx}}{\partial x} + \delta \frac{\partial \sigma^V_{zz}}{\partial z} = 0. \tag{A26}$$

Now we asymptotically expand the dependent variables in powers of $\delta = \hat{h}/L$. For example,

$$u = u_0(x, z, t) + \delta u_1(x, z, t) + \delta^2 u_2(x, z, t) + \cdots,$$

and we do the same for θ, v, p, and h. We substitute these into the governing equations and boundary conditions, and then collect like powers of δ. Then at $O(1)$, the equations inside the sheet, $-h_0/2 < z < h_0/2$, are

$$\frac{1}{2}(\alpha_2 + \alpha_3 - \alpha_5 + \alpha_6 + 2\alpha_1 \cos 2\theta_0)\sin 2\theta_0 u_{0z}\theta_{0z} - \hat{N}\theta_{0z}\theta_{0zz}$$
$$+\frac{1}{2}\left[2 + (\alpha_5 - \alpha_2)\cos^2\theta_0 + (\alpha_3 + \alpha_6)\sin^2\theta_0 + \frac{1}{2}\alpha_1 \sin^2 2\theta_0\right]$$
$$u_{0zz} = 0, \tag{A27}$$

$$-\hat{N}\theta_{0z}\theta_{0zz} = 0, \tag{A28}$$

$$\hat{N}\theta_{0zz} = 0, \tag{A29}$$

$$u_{0x} + w_{0z} = 0. \tag{A30}$$

On the sheet surface $z = h_0/2$, the $O(1)$ equations are

$$-\hat{N}\theta_{0z}^2 = 0, \tag{A31}$$

$$\frac{1}{2}\left[2 + (\alpha_5 - \alpha_2)\cos^2\theta_0 + (\alpha_3 + \alpha_6)\sin^2\theta_0 + \frac{1}{2}\alpha_1 \sin^2 2\theta_0\right]u_{0z}$$
$$-\frac{1}{2}\hat{N}\theta_{0z}^2 h_{0x} - \hat{N}\theta_{0z}\theta_{0x} = 0, \tag{A32}$$

$$w_0 - \frac{1}{2}(h_{0t} + u_0 h_{0x}) = 0, \tag{A33}$$

$$\theta_0 - \theta_B = 0. \tag{A34}$$

In order, these equations represent momentum in the x and z-components respectively; energy; and continuity; followed by the boundary conditions on the top surface: normal and tangential stress, kinematic, and anchoring. Solving these leading order equations, we obtain

$$\theta_0 = \theta_B, \tag{A35}$$

$$u_0 = u_0(x, t), \tag{A36}$$

$$w_0 = w_0(x, z, t) = -u_{0x}z, \tag{A37}$$

$$h_{0t} + (u_0 h_0)_x = 0, \tag{A38}$$

where Eq. (A38) is the mass balance equation and Eq. (A37) is the transverse velocity. As is typical in such flow models, we get a simple leading order equation for the transverse velocity that comes from integrating mass conservation Eq. (A30); the axial velocity u is independent of depth, and so w_0 is a linear function of z. At $O(1)$, we cannot determine u_0, so to close the system, we continue on to order δ. After making the above substitutions, the $O(\delta)$ equations inside the sheet, $-h_0/2 < z < h_0/2$, are

$$\frac{1}{8}[8 + \alpha_1 - 2(\alpha_2 + \alpha_3 + \alpha_5 + \alpha_6) - 2(\alpha_2 + \alpha_3 - \alpha_5 + \alpha_6)\cos 2\theta_B$$
$$-\alpha_1 \cos 4\theta_B]u_{1zz} - p_{0x} = 0, \tag{A39}$$

$$p_{0z} = 0, \tag{A40}$$

$$\hat{N}\theta_{1zz} = 0, \tag{A41}$$

$$u_{1x} + w_{1z} = 0. \tag{A42}$$

On the sheet surface $z = h_0/2$, the $O(\delta)$ equations are

$$p_0 + \frac{S}{2}h_{0xx} = 0, \tag{A43}$$

$$-\frac{1}{2}(\alpha_1 \cos 2\theta_B - \alpha_5 + \alpha_6)\sin 2\theta_B u_{0x} + \frac{1}{4}\left[4 - 2(\alpha_2 - \alpha_5)\cos^2\theta_B\right.$$
$$\left. + 2(\alpha_3 + \alpha_6)\sin^2\theta_B + \alpha_1 \sin^2 2\theta_B\right]u_{1z} = 0, \tag{A44}$$

$$w_1 - \frac{1}{2}(h_{1t} + u_1 h_{0x} + u_0 h_{1x}) = 0, \tag{A45}$$

$$\theta_1 = 0. \tag{A46}$$

Solving, we obtain

$$p_0(x, t) = -\frac{S}{2}h_{0xx}, \tag{A47}$$

$$u_1(x, z, t) = \frac{p_{0x}}{F(\theta_B)}\left(\frac{z^2}{2} - \frac{h_0}{2}z\right) - \frac{A(\theta_B, u_{0x})}{B(\theta_B)}z + K(x, t), \tag{A48}$$

$$\theta_1(x, z, t) = 0, \tag{A49}$$

where

$$A(\theta_B, u_{0x}) = 2(\alpha_1 \cos 2\theta_B - \alpha_5 + \alpha_6)\sin 2\theta_B u_{0x}, \tag{A50}$$

$$B(\theta_B) = \alpha_1 \sin^2 2\theta_B - 2(\alpha_2 - \alpha_5)\cos^2\theta_B + 2(\alpha_3 + \alpha_6)\sin^2\theta_B + 4, \tag{A51}$$

and $K(x, t)$ is as yet unknown. To close the system, we must proceed to $O(\delta^2)$ to find an equation for u_0. We make the above substitutions, in addition to the substitution $w_{1zz} = -u_{1xz}$, obtained from differentiating the continuity equation. At this order, the equations are too long to be profitably displayed in their entirety, so we summarize the steps. First, we use z-momentum and the normal stress condition to determine

$$p_1(x, z, t) = G_1(\theta_B)u_{0x} + H_1(\theta_B)S(2z - h_0)h_{0xxx} - \frac{S}{2}h_{1xx}, \tag{A52}$$

where

$$G_1(\theta_B) = \frac{1}{4}\left[-8 - \alpha_1 - 2\alpha_5 - 2\alpha_6 - 2(\alpha_1 + \alpha_5 + \alpha_6)\cos 2\theta_B - \alpha_1 \cos 4\theta_B\right]$$
$$+ \frac{(-\alpha_1 - \alpha_2 - \alpha_3 - \alpha_5 - \alpha_6 - \alpha_1 \cos 2\theta_B)(-\alpha_5 + \alpha_6 + \alpha_1 \cos 2\theta_B)\sin 2\theta_B^2}{8 + \alpha_1 - 2\alpha_2 + 2\alpha_3 + 2\alpha_5 + 2\alpha_6 - 2(\alpha_2 + \alpha_3 - \alpha_5 + \alpha_6)\cos 2\theta_B - \alpha_1 \cos 4\theta_B},$$
$$H_1(\theta_B) = \frac{(-\alpha_1 - \alpha_2 - \alpha_3 - \alpha_5 - \alpha_6 - \alpha_1 \cos 2\theta_B)\sin 2\theta_B}{2[8 + \alpha_1 - 2\alpha_2 + 2\alpha_3 + 2\alpha_5 + 2\alpha_6 - 2(\alpha_2 + \alpha_3 - \alpha_5 + \alpha_6)\cos 2\theta_B - \alpha_1 \cos 4\theta_B]}.$$

Then, substituting p_1 and others into x-momentum Eq. (A40), we solve for u_{2zz} and integrate across the sheet. From the tangential stress condition we obtain the solvability condition, which leads to

$$\frac{B_2(\theta_B)}{A_2(\theta_B)}(h_0 u_{0x})_x + \frac{C_2(\theta_B)}{A_2(\theta_B)}S(h_0^2 h_{0xxx})_x + 4Sh_0 h_{1xxx} = 0, \tag{A53}$$

where

$$A_2(\theta_B) = 8 + \alpha_1 - 2\alpha_2 + 2\alpha_3 + 2\alpha_5 + 2\alpha_6,$$
$$- 2(\alpha_2 + \alpha_3 - \alpha_5 + \alpha_6)\cos 2\theta_B - \alpha_1 \cos 4\theta_B, \tag{A54}$$

$$B_2(\theta_B) = -4[2\alpha_1\alpha_2 + 2\alpha_1\alpha_3 - 2\alpha_1\alpha_5 + 2\alpha_1\alpha_6]\cos 6\theta_B$$
$$- 4\big[-64 - 16\alpha_1 - \alpha_1^2 + 16\alpha_2 + 2\alpha_1\alpha_2 - 16\alpha_3 - 2\alpha_1\alpha_3$$
$$- 32\alpha_5 - 4\alpha_1\alpha_5 + 6\alpha_2\alpha_5 - 2\alpha_3\alpha_5 - 4\alpha_5^2 - 32\alpha_6 - 4\alpha_1\alpha_6$$
$$+ 2\alpha_2\alpha_6 - 6\alpha_3\alpha_6 - 8\alpha_5\alpha_6 - 4\alpha_6^2 + 2(\alpha_2 + \alpha_3 - \alpha_5 + \alpha_6)$$
$$\times (\alpha_1 + 2[4 + \alpha_5 + \alpha_6])\cos 2\theta_B + 2(\alpha_1[\alpha_2 - \alpha_3]$$
$$- [\alpha_2 + \alpha_3][\alpha_5 - \alpha_6])\cos 4\theta_B + \alpha_1^2 \cos 8\theta_B\big], \tag{A55}$$

$$C_2(\theta_B) = -8(\alpha_2 + \alpha_3 + \alpha_1 \cos 2\theta_B)\sin \theta_B. \tag{A56}$$

Note that the undetermined function $K(x, t)$ from u_1 does not appear in the solvability condition. However, if take the continuity equation from $O(\delta)$, integrate with respect to z, and apply the kinematic boundary conditions, we find

$$h_{1t} + u_0 h_{1x} + [h_0 K(x, t)]_x - \frac{S}{6A_2(\theta_B)}(h_0^3 h_{0xxx})_x = 0, \tag{A57}$$

where $A_2(\theta_B)$ is as defined above.

As observed by Howell,[67] the $O(\delta)$ term for h does not contribute to the derivation of the leading order problem, and so

$$h(x, t) = h_0(x, t) + \delta^2 h_2(x, t) + O(\delta^3). \tag{A58}$$

Then Eqs. (A38), (A53), and (A57) simplify to

$$h_{0t} + (u_0 h_0)_x = 0, \tag{A59}$$

$$B_2(\theta_B)(h_0 u_{0x})_x + C_2(\theta_B)S(h_0^2 h_{0xxx})_x = 0, \tag{A60}$$

$$[h_0 K(x, t)]_x - \frac{S}{6A_2(\theta_B)}(h_0^3 h_{0xxx})_x = 0. \tag{A61}$$

We thus have three equations with three unknowns: $u_0(x, t)$, $h_0(x, t)$, and $K(x, t)$. We solve for $K(x, t)$ by integrating Eq. (A61) with respect to x. We determine the constant of integration by integrating u_1 through the depth; no net flux along the film due to u_1 results in

$$K(x, t) = \frac{S}{2}\frac{h_0^2 h_{0xxx}}{3A_2(\theta_B)}, \tag{A62}$$

$$u_1(x, z, t) = \frac{p_{0x}}{F(\theta_B)}\left(\frac{z^2}{2} - \frac{h_0}{2}z\right) - \frac{A(\theta_B, u_{0x})}{B(\theta_B)}z + \frac{S}{2}\frac{h_0^2 h_{0xxx}}{3A_2(\theta_B)}. \tag{A63}$$

Using u_1, we can solve mass conservation Eq. (A42) to find w_1. This term will be a cubic in z, and will thus be smooth and bounded. As a result, the term δw_1 remains small and will not affect the leading order dynamics. Then, to find the axial velocity u_0 and the sheet thickness h_0, we can solve the coupled system

$$h_{0t} + (u_0 h_0)_x = 0, \tag{A64}$$

$$(h_0 u_{0x})_x + \tilde{S}(h_0^2 h_{0xxx})_x = 0, \tag{A65}$$

where

$$\tilde{S} = \frac{C_2(\theta_B)}{B_2(\theta_B)}S. \tag{A66}$$

In the paper we take $\tilde{S} = S$.

APPENDIX B: VALIDATION OF NUMERICAL METHODS

When solving the system numerically, we discretized over $0 \le \xi \le 1$ using both finite difference with uniform spacing $\Delta\xi = 1/n$ and Chebyshev spectral discretizations using $m + 1$ (mapped) Chebyshev points. We validated the two methods using solutions obtained for the thickness of the sheet in the case of weak elasticity with BC case I, an initial condition containing one wave ($k_0 = 1$), $v_0 = 1$, and $S = 0.0025$, using increasing resolution. For the finite difference method we compared solutions from grids with $n = 64, 96, 128, 256,$ and 512; for the spectral method, we used $m = 64, 96,$ and 128. First, all solutions were interpolated onto a uniform grid of with $n = 512$. Then, we calculated the relative error estimate at the final time of $t = 3$, using the finest resolution for the respective method as the reference. So for example, for the spectral method, the relative error estimate using $m = 64$ was calculated as

$$\frac{||h_{sp,128} - h_{sp,64}||_2}{||h_{sp,128}||_2},$$

where $h_{sp,64}$ represents the solution vector obtained with that spacing at the final time. The results are shown in Table VII, and verify that both methods are converging.

TABLE VII. Comparison of the relative error estimate of finite difference and Chebyshev spectral discretization. For the finite difference method, the slope of a linear fit to the errors on a log–log plot is −2.2, verifying second order convergence.

Grid size	Relative error estimate	
	Spectral	Finite difference
64	1.53×10^{-4}	8.56×10^{-4}
96	1.13×10^{-6}	3.73×10^{-4}
128	$\cdots$	2.04×10^{-4}
256	$\cdots$	4.08×10^{-5}

REFERENCES

[1] R. J. Braun, P. E. King-Smith, C. G. Begley, L. Li, and N. R. Gewecke, "Dynamics and function of the tear film in relation to the blink cycle," Prog. Retinal Eye Res. **45**, 132–164 (2015).

[2] M. Willcox, P. Argüeso, G. Georgiev, J. Holopainen, G. Laurie, T. Millar, E. Papas, J. Rolland, T. Schmidt, U. Stahl, T. Suarez, L. Subbaraman, O. Ucakhan, and L. Jones, "TFOS DEWS-II tear film report," Ocul. Surf. **15**, 369–403 (2017).

[3] P. E. King-Smith, J. J. Nichols, K. K. Nichols, and R. J. Braun, "A high resolution microscope for imaging the lipid layer of the tear film," Ocul. Surf. **9**, 197–211 (2011).

[4] P. E. King-Smith, B. A. Fink, R. M. Hill, K. W. Koelling, and J. M. Tiffany, "The thickness of the tear film," Curr. Eye Res. **29**, 357–368 (2004).

[5] A. Bron, J. Tiffany, S. Gouveia, N. Yokoi, and L. Voon, "Functional aspects of the tear film lipid layer," Exp. Eye Res. **78**, 347–360 (2004).

[6] I. K. Gipson, "Distribution of mucins at the ocular surface," Exp. Eye Res. **78**, 379–388 (2004).

[7] B. Govindarajan and I. Gipson, "Membrane-tethered mucins have multiple functions on the ocular surface," Exp. Eye Res. **90**, 655–693 (2010).

[8] A. Bron, P. Argüeso, M. Irkec, and F. V. Bright, "Clinical staining of the ocular surface: Mechanisms and interpretations," Prog. Retinal Eye Res **44**, 36–61 (2015).

[9] M. Fini, S. Jeong, H. Gong, R. Martinez-Carrasco, N. Laver, M. Hijikata, N. Keicho, and P. Argüeso, "Membrane-associated mucins of the ocular surface: New genes, new protein functions and new biological roles in human and mouse," Prog. Retinal Eye Res. **75**, 100777 (2020).

[10] M. Hogan, J. Alvarado, and J. Weddell, *Histology of the Human Eye* (W.B. Saunders, Philadelphia, 1971).

[11] P. E. King-Smith, C. G. Begley, and R. J. Braun, "Mechanisms, imaging and structure of tear film breakup," Ocul. Surf. **16**, 4–30 (2018).

[12] N. Yokoi, G. A. Georgiev, H. Kato, A. Komuro, Y. Sonomura, C. Sotozono, K. Tsubota, and S. Kinoshita, "Classification of fluorescein breakup patterns: A novel method of differential diagnosis for dry eye," Am. J. Ophthalmol. **180**, 72–85 (2017).

[13] J. P. Gilbard, R. L. Farris, and J. Santamaria, "Osmolarity of tear microvolumes in keratoconjunctivitis sicca," Arch. Ophthalmol. **96**, 677–681 (1978).

[14] C. Baudouin, P. Aragona, E. M. Messmer, A. Tomlinson, M. Calonge, K. G. Boboridis, Y. A. Akova, G. Geerling, M. Labetoulle, and M. Rolando, "Role of hyperosmolarity in the pathogenesis and management of dry eye disease: Proceedings of the OCEAN group meeting," Ocul. Surf. **11**, 246–258 (2013).

[15] J. P. Craig, K. K. Nichols, E. K. Akpek, B. Caffery, H. S. Dua, C.-K. Joo, Z. Liu, J. D. Nelson, J. J. Nichols, K. Tsubota *et al.*, "TFOS DEWS-II definition and classification report," Ocul. Surf. **15**, 276–283 (2017).

[16] P. E. King-Smith, K. S. Reuter, R. J. Braun, J. J. Nichols, and K. K. Nichols, "Tear film breakup and structure studied by simultaneous video recording of fluorescence and tear film lipid layer, TFLL, images," Invest. Ophthalmol. Vis. Sci. **54**, 4900–4909 (2013).

[17] S. Mishima and D. Maurice, "The oily layer of the tear film and evaporation from the corneal surface," Exp. Eye Res. **1**, 39–45 (1961).

[18] P. E. King-Smith, E. A. Hinel, and J. J. Nichols, "Application of a novel interferometric method to investigate the relation between lipid layer thickness and tear film thinning," Invest. Ophthalmol. Vis. Sci. **51**, 2418–2423 (2010).

[19] I. A. Butovich, H. Lu, A. McMahon, H. Ketelson, M. Senchyna, D. Meadows, E. Campbell, M. Molai, and E. Linsenbardt, "Biophysical and morphological evaluation of human normal and dry eye meibum using hot stage polarized light microscopy," Invest. Ophthalmol. Vis. Sci. **55**, 87–101 (2014).

[20] D. L. Leiske, C. I. Leiske, D. R. Leiske, M. F. Toney, M. Senchyna, H. A. Ketelson, D. L. Meadows, and G. G. Fuller, "Temperature-induced transitions in the structure and interfacial rheology of human meibum," Biophys. J. **102**, 369–376 (2012).

[21] D. L. Leiske, C. E. Miller, L. Rosenfeld, C. Cerretani, A. Ayzner, B. Lin, M. Meron, M. Senchyna, H. A. Ketelson, D. Meadows, S. Srinivasan, L. Jones, C. J. Radke, M. F. Toney, and G. G. Fuller, "Molecular structure of interfacial human meibum films," Langmuir **28**, 11858–11865 (2012).

[22] L. Rosenfeld, C. Cerretani, D. L. Leiske, M. F. Toney, C. J. Radke, and G. G. Fuller, "Structural and rheological properties of meibomian lipid," Invest. Ophthalmol. Vis. Sci. **54**, 2720–2732 (2013).

[23] E. Knop, N. Knop, T. Millar, H. Obata, and D. Sullivan, "The international workshop on meibomian gland dysfunction: Report of the subcommittee on anatomy, physiology, and pathophysiology of the meibomian gland," Invest. Ophthalmol. Vis. Sci. **52**, 1938–1978 (2011).

[24] P. Sirigu, R.-L. Shen, and P. da Silva, "Human meibomian glands: The ultrastucture of acinar cells as viewed by thin section and freeze-fracture transmission electron microscopies," Invest. Ophthalmol. Vis. Sci. **33**, 2284–2292 (1992).

[25] P. E. King-Smith, M. D. Bailey, and R. J. Braun, "Four characteristics and a model of an effective tear film lipid layer," Ocul. Surf. **11**, 236–245 (2013).

[26] J. C. Pandit, B. Nagyová, A. J. Bron, and J. M. Tiffany, "Physical properties of stimulated and unstimulated tears," Exp. Eye Res. **68**, 247–253 (1999).

[27] G. Georgiev, D. Borchman, P. Eftimov, and N. Yokoi, "Lipid saturation and the rheology of human tear lipids," Int. J. Molec. Sci. **20**, 3431 (2019).

[28] D.-K. Yang and S.-T. Wu, *Fundamentals of Liquid Crystal Devices*, 2nd ed. (Wiley, Chichester, 2015).

[29] N. Efron, G. Young, and N. A. Brennan, "Ocular surface temperature," Curr. Eye Res. **8**, 901–906 (1989).

[30] J. P. Craig, I. Singh, A. Tomlinson, P. B. Morgan, and N. Efron, "The role of tear physiology in ocular surface temperature," Eye **14**, 635–641 (2000).

[31] C. Purslow and J. S. Wolffsohn, "Ocular surface temperature: A review," Eye Contact Lens **31**, 117–123 (2005).

[32] Q. Deng, R. J. Braun, T. A. Driscoll, and P. E. King-Smith, "A model for the tear film and ocular surface temperature for partial blinks," Interfacial Phenom. Heat Transfer. **1**, 357–381 (2013).

[33] Q. Deng, R. J. Braun, and T. A. Driscoll, "Heat transfer and tear film dynamics over multiple blink cycles," Phys. Fluids **26**, 071901 (2014).

[34] C. J. Petrie, "One hundred years of extensional flow," J. Nonnewton. Fluid Mech. **137**, 1–14 (2006).

[35] P. D. Howell, "Extensional thin layer flows," Ph.D. thesis (Oxford University, Oxford, UK, 1994).

[36] W. W. Schultz and S. H. Davis, "One-dimensional liquid fibers," J. Rheol. **26**, 331–345 (1982).

[37] J. N. Dewynne, J. R. Ockendon, and P. Wilmott, "A systematic derivation of the leading-order equations for extensional flows in slender geometries," J. Fluid Mech. **244**, 323–338 (1992).

[38] J. N. Dewynne, P. D. Howell, and P. Wilmott, "Slender viscous fibres with inertia and gravity," Q. J. Mech. Appl. Math. **47**, 541–555 (1994).

[39] J. J. Wylie, H. Huang, and R. M. Miura, "Stretching of viscous threads at low Reynolds numbers," J. Fluid Mech. **683**, 212–234 (2011).

[40] C. Clasen, J. Eggers, M. A. Fontelos, J. Li, and G. H. McKinley, "The beads-on-string structure of viscoelastic threads," J. Fluid Mech. **556**, 283–308 (2006).

[41] M. C. Sostarecz and A. Belmonte, "Beads-on-string phenomena in wormlike micellar fluids," Phys. Fluids **16**, L67–L70 (2004).

[42] L. B. Smolka, A. Belmonte, D. M. Henderson, and T. P. Witelski, "Exact solution for the extensional flow of a viscoelastic filament," Eur. J. Appl. Math. **15**, 679–712 (2004).

[43] L. J. Cummings, J. Low, and T. G. Myers, "Extensional flow of nematic liquid crystal with an applied electric field," Eur. J. Appl. Math. **25**, 397–423 (2014).

[44] T.-S. Lin, L. J. Cummings, A. J. Archer, L. Kondic, and U. Thiele, "Note on the hydrodynamic description of thin nematic films: Strong anchoring model," Phys. Fluids **25**, 082102 (2013).

[45] M. A. Lam, L. J. Cummings, T.-S. Lin, and L. Kondic, "Modeling flow of nematic liquid crystal down an incline," J. Eng. Math. **94**, 97–113 (2015).

[46] F. M. Leslie, "Theory of flow phenomena in liquid crystals," in *Advances in Liquid Crystals* (Elsevier, 1979), Vol. 4, pp. 1–81.

[47] I. W. Stewart, *The Static and Dynamic Continuum Theory of Liquid Crystals: A Mathematical Introduction* (CRC Press, 2019).

[48] M. G. Doane, "Interactions of eyelids and tears in corneal wetting and the dynamics of the normal human eyeblink," Am. J. Ophthalmol. **89**, 507–516 (1980).

[49] L. W. Honaker, A. Sharma, A. Schanen, and J. P. Lagerwall, "Measuring the anisotropy in interfacial tension of nematic liquid crystals," Crystals **11**, 687 (2021).

[50] F. T. Trouton, "On the coefficient of viscous traction and its relation to that of viscosity," Proc. R. Soc. A **77**, 426–440 (1906).

[51] L. M. Tarakhan, "Determination of the surface tension of 5CB liquid crystal by the pendant drop method," Ukr. Fiz. Zhur. **51**, 22–26 (2006).

[52] C.-C. Peng, C. Cerretani, R. J. Braun, and C. J. Radke, "Evaporation-driven instability of the precorneal tear film," Adv. Colloid Interface Sci. **206**, 250–264 (2014).

[53] L. N. Trefethen, *Spectral Methods in MATLAB* (SIAM, Philadelphia, 2000).

[54] M. B. Jones, D. L. S. McElwain, G. R. Fulford, M. J. Collins, and A. P. Roberts, "The effect of the lipid layer on tear film behaviour," Bull. Math. Biol. **68**, 1355–1381 (2006).

[55] M. B. Jones, C. P. Please, D. L. S. McElwain, G. R. Fulford, A. P. Roberts, and M. J. Collins, "Dynamics of tear film deposition and draining," Math. Med. Biol. J. IMA **22**, 265–288 (2005).

[56] A. Heryudono, R. J. Braun, T. A. Driscoll, K. L. Maki, L. P. Cook, and P. E. King-Smith, "Single-equation models for the tear film in a blink cycle: Realistic lid motion," Math. Med. Biol. J. IMA **24**, 347–377 (2007).

[57] K. L. Maki, R. J. Braun, T. A. Driscoll, and P. E. King-Smith, "An overset grid method for the study of reflex tearing," Math. Med. Biol. **25**, 187–214 (2008).

[58] L. Jossic, P. Lefevre, C. de Loubens, A. Magnin, and C. Corre, "The fluid mechanics of shear-thinning tear substitutes," J. Non-Newtonian Fluid Mech. **161**, 1–9 (2009).

[59] E. Aydemir, C. J. W. Breward, and T. P. Witelski, "The effect of polar lipids on tear film dynamics," Bull. Math. Biol. **73**, 1171–1201 (2011).

[60] M. Allouche, H. A. Abderrahmane, S. M. Djouadi, and K. Mansouri, "Influence of curvature on tear film dynamics," Eur. J. Mech. B Fluids **66**, 81–91 (2017).

[61] H. Mehdaoui, H. A. Abderrahmane, F. N. Bouda, and A. Koulali, "2D numerical simulation of tear film dynamics: Effects of shear-thinning properties," Eur. J. Mech. B Fluids **90**, 128–136 (2021).

[62] A. Oron, S. H. Davis, and S. G. Bankoff, "Long-scale evolution of thin liquid films," Rev. Mod. Phys. **69**, 931–980 (1997).

[63] A. L. Bertozzi, M. P. Brenner, T. F. Dupont, and L. P. Kadanoff, "Singularities and similarities in interface flows," in *Trends and Perspectives in Applied Mathematics, Applied Mathematical Sciences*, edited by L. Sirovich (Springer-Verlag, New York, 1994), Vol. 100, pp. 155–208.

[64] M. Bruna and C. J. W. Breward, "The influence of non-polar lipids on tear film dynamics," J. Fluid Mech. **746**, 565–605 (2014).

[65] M. R. Stapf, R. J. Braun, and P. E. King-Smith, "Duplex tear film evaporation analysis," Bull. Math. Biol. **79**, 2814–2846 (2017).

[66] V. S. Zubkov, C. J. W. Breward, and E. A. Gaffney, "Coupling fluid and solute dynamics within the ocular surface tear film: A modelling study of black line osmolarity," Bull. Math. Biol. **74**, 2062–2093 (2012).

[67] P. D. Howell, "Models for thin viscous sheets," Eur. J. Appl. Math. **7**, 321–343 (1996).